THESIS FOR THE DEGREE OF DOCTOR OF PHILOSOPHY

Magnetotransport characterization of epitaxial graphene on SiC

Samuel Alejandro Lara Avila

CHALMERS

Department of Microtechnology and Nanoscience-MC2

CHALMERS UNIVERSITY OF TECHNOLOGY

Göteborg, Sweden 2012

Magnetotransport characterization of epitaxial graphene on SiC
Samuel Alejandro Lara Avila
ISBN 978-91-7385-700-0

Doktorsavhandlingar vid Chalmers tekniska högskola: 0346-718X
Ny serie nr 3381
ISSN 0346-718X

Chalmers University of Technology
Department of Microtechnology and Nanoscience
Quantum Device Physics Laboratory
Experimental Mesoscopic Physics Group
SE-412 96 Göteborg, Sweden
Telephone: + 46 31 - 772 1000

ISSN 1652-0769
Technical Report MC2-224

Chalmers Reproservice
Göteborg, Sweden 2012

Magnetotransport characterization of epitaxial graphene on SiC
Samuel Alejandro Lara Avila
Department of Microtechnology and Nanoscience
Chalmers University of Technology, 2012

Abstract

Low-temperature magnetotransport is used to characterize graphene grown epitaxially on the silicon face of 4H silicon carbide (SiC/G). Transport measurements suggest that a graphene monolayer grows continuosly over the characteristic terraces of the SiC susbtrate, as confirmed by half-integer quantum Hall effect (QHE) observed in large Hall bars patterned across several terraces.

Complete characterization was possible using carrier density control technologies developed for SiC/G, including organic dielectrics, photochemical gating and a solid electrolyte. The photochemical gating with organic polymers, achieved by using a spacer layer directly in contact with graphene that protects its integrity, followed by a layer that responds to light, is envisioned as a prototypical architecture for the development of graphene-based sensors.

Fine details of electron scattering were found through measurement of quantum corrections to the conductivity of SiC/G, arising from weak localization (WL) and electron-electron interactions (E-E). It was found that scattering is determined by charged impurities under graphene, while the effect of terraces manifests as intervalley scattering; the extracted temperature dependence of the decoherence rate allowed to identify electron-electron interactions and to suggest spin-flip centers as sources of dephasing in the system. The analysis of WL provided an indirect measurement of the spin relaxation time in SiC/G, at the level of 50 ps.

Altogether, this work contributed to develop the first application in which graphene outperforms conventional semiconducors, in the field of quantum metrology. The half integer QHE in SiC/G is proposed as standard for electrical resistance to replace GaAs heterostructures. A direct comparison with the QHE in GaAs, the most strict universality test of the QHE ever performed, supports the hypothesis that the electrical resistance is quantized in units of h/e^2, with an uncertainty of 0.084 parts per billion. The accuracy of the comparison was limited by the critical current in the GaAs sample, 4 times lower than in the SiC/G sample.

Keywords: Carbon-based materials, electronic transport, epitaxial graphene, quantum Hall effect, magnetotransport, weak localization, many-electron systems.

List of publications

This thesis is based on the work contained in the following papers:

I: Towards a quantum resistance standard based on epitaxial graphene
A.Tzalenchuk, S. Lara-Avila, A. Kalaboukhov, S. Paolillo, M. Syväjärvi , R. Yakimova, O. Kazakova, T.J.B.M. Janssen, V. Fal'ko, and S. Kubatkin.
Nature Nanotechnology, 5, 186-9, (2010).

II: Anomalously strong pinning of the filling factor $\nu = 2$ in epitaxial graphene
T. J.B.M. Janssen, A. Tzalenchuk, R. Yakimova, S. Kubatkin, S. Lara-Avila, S. Kopylov, and V. Fal'ko
Physical Review B, 83, 233402, (2011).

III: Non-volatile photochemical gating of an epitaxial graphene/polymer heterostructure
S. Lara-Avila, K. Moth-Poulsen, R. Yakimova, T Bjørnholm, V. Fal'ko, A. Tzalenchuk, and S. Kubatkin
Advanced Materials, 23, 878882, (2011)

IV: Disordered Fermi liquid in epitaxial graphene from quantum transport measurements
S. Lara-Avila, A. Tzalenchuk, S. Kubatkin, R. Yakimova, TJBM Janssen, K. Cedergren, T. Bergsten, and Vladimir Fal'ko.
Physical Review Letters, 107, 1-5 (2011).

V: Engineering and metrology of epitaxial graphene
A. Tzalenchuk, S. Lara-Avila, K. Cedergren, M. Syväjärvi, R. Yakimova, O. Kazakova, T.J.B.M. Janssen, K. Moth-Poulsen, T. Bjørnholm, S. Kopylov, V. Fal'ko, and S. Kubatkin
Solid State Communications, 151, 10941099, (2011).

Contents

Contents **v**

1 Introduction **1**

2 Concepts **7**

2.1 Magnetotransport in 2D semiconductors 7

2.1.1 Hall effect 8

2.1.2 High magnetic fields 8

2.1.3 Integer quantum Hall effect (QHE) 10

2.1.4 Quantum interference 12

2.2 Graphene 14

2.2.1 Crystal and electronic Structure 14

2.2.2 Low-energy spectrum 17

2.3 Magnetotransport in graphene 18

2.3.1 Half-Integer quantum Hall effect 19

2.3.2 Weak (anti) localization in graphene 20

3 Experimental Techniques **25**

3.1 Microfabrication 26

3.2 Magnetotransport 27

3.3 Measuring Decoherence 28

3.4 Fits to weak localization theory 29

3.5 Metrological techniques 31

4 The quest for monolayer graphene on silicon carbide **33**
4.1 Making electronic-grade graphene 34
4.2 The precursor: crystal structure of SiC 35
4.3 Multilayer graphene on the C-face 35
4.4 Single-layer graphene on the Si-face (SiC/G) 37
4.5 Magnetotransport in SiC/G 38
4.6 Summary 42

5 Carrier density control in SiC/G **45**
5.1 Encapsulation with organic polymers 46
5.2 Electrostatic carrier control 47
5.3 Photochemical gating 48
5.4 Solid electrolyte 50
5.5 Summary 53

6 Quantum corrections to charge transport in SiC/G **55**
6.1 Electron scattering in SiC/G 56
6.2 Experimental steps 56
6.3 Weak Localization Effects 57
6.4 Electron-electron interaction effects 60
6.5 Summary 64

7 Quantum Metrology with SiC/G **67**
7.1 The need for metrology 68
7.2 Quantum Hall effect for electrical resistance standard 70
7.3 Why graphene? 70
7.4 Quantum Metrology with SiC/G 73
7.5 Comparison of SiC/G and GaAs Heterostructure 75
7.6 Summary 76

8 Summary & Outlook **79**

Appendix A:Sample Preparation **83**

References **89**

Chapter 1

Introduction

Graphene was the first two-dimensional crystal to become experimentally available [1, 2]. Before graphene, two-dimensional systems were formed and studied at low temperatures by confining electrons at interfaces of, for example, Si/SiO_2 or AlGaAs/GaAs.

Many interesting properties of graphene were predicted long before and perhaps more important, confirmed after its experimental discovery. Its band structure was unveiled as early as in 1946 [3], and its linear E(k) spectrum and chiral, pseudo-relativistic carriers were confirmed after it was isolated for the first time in 2004 by cleaving graphite [1, 2]. The exotic electronic structure together with unique properties such as high thermal conductivity, high current density capability, optical transparency, etc., put forth graphene as a remarkably interesting material not only for fundamental physics but also for numerous applications.

Future electronic applications

Monolayer graphene has been envisioned as a successor to silicon. The vanishing density of states at the Dirac point and high carrier mobilities suggested that graphene field effect transistors would be fast and display large on/off ratios, useful for logic applications. In reality it has been found that even when the chemical potential of a graphene sample is close to the Dirac point, there exist domains of electrons and holes, so-called puddles. The overall consequence of this inhomogeneous doping profile along graphene is that it displays a maximum

resistance of ~ 6 kΩ/square, which is not sufficiently "off" for digital electronics.

One application for which graphene is a decent contender is high frequency analogue electronics. The bipolarity of a graphene transistor, the fact that its resistance at a given carrier concentration is the same for electrons as it is for holes $R(n) = R(-n)$, has been exploited to fabricate devices with cut-off frequency as high as 100 GHz [4, 5].

In addition to its exotic electronic structure, being optically transparent while still electrically conductive makes graphene a very attractive material in opto-electronics. Graphene could be used as replacement for Indium Tin Oxide, an expensive and scarce material employed in transparent electrodes.

Large-area graphene

Nowadays there are several ways to produce monolayer graphene, and each technique produces a "different" graphene that is suitable for different purposes. Graphene flakes obtained by exfoliation of graphite continue to display the best electron mobilities, but their small size limit their use to the scientific playground.

From an application point of view, producing graphene on large-area substrates would enable mass fabrication of graphene-based devices. There are currently two methods for producing large-area graphene: 1) decomposing organic compounds on catalytic metals followed by graphitization (CVD) and 2) epitaxial growth on silicon carbide (SiC) by silicon sublimation at high temperatures. Graphene grown by CVD is cheap but polycrystalline (low mobility) while epitaxial graphene on SiC is expensive but provides fairly good carrier mobilities (up to an order of magnitude better than silicon). Thus, epitaxial graphene is a candidate for high-performance applications.

Counting the layers

Since graphene is only one-atom thin (≈ 4 Å), quality control of graphene by optical inspection is cumbersome as it reflects only 2.3% of the incident light [6]. When placed on silicon crystals coated with an oxide layer either 90 or 300 nm thick, thin graphite flakes and even monolayer graphene can be observed with a simple optical microscope due to interference; this effect led to its discovery. A

skilled person can distinguish the number of layers in a particular flake, but no more information than this can be retrieved.

There exist other surface characterization tools suitable for evaluating the quality of graphene. Atomic force microscopy can provide information about the height, continuity and rugosity of the layer. The presence or absence of certain peaks in the Raman spectrum reveals the monolayer character as well as the amount of disorder. Finally, angle-resolved photo electron spectroscopy (ARPES) provide direct information of the band structure, in which a linear $E(k)$ corresponds to monolayer graphene.

A powerful yet simple technique for characterization of graphene is magnetotransport measurements. When placed in crossed electric and magnetic fields, the peculiar electronic structure of graphene manifests in novel and unique features, such as the half-integer quantum Hall effect at high magnetic fields and low temperatures, the fingerprint of monolayer graphene. The sequence of plateaux in the quantum Hall regime, different for one, two or more layers is an infallible way to distinguish the number of layers that contribute to electron transport. Additionally, at low magnetic field, room temperature Hall effect measurements reveal the carrier type (electron or hole), mobilities, concentration and relaxation times. Magnetotransport thus allows to distinguish not only the number of graphene layers, but also to assess their quality in terms of electronic transport properties.

The quest for monolayer graphene on silicon carbide (SiC)

The first attempt to produce monolayer graphene on SiC was reported in 2004; in this, $2-4$ monolayers were obtained [7]. Several failed attempts followed the initial report [8–10], revealing that the quality of the as-grown layers depend on several parameters, including the conditions used during growth, the particular structure of the SiC crystal and which "side" of the crystal was used: the silicon or the carbon face. Graphene grows faster on the carbon face, leading to a difficult growth control which results in multilayer graphene. On the silicon face, graphene islands were found when SiC was annealed in vacuum.

The group of Rositza Yakimova[1] pioneered growth at high temperature and pressure instead of vacuum ($T = 2000^o$ C, $P = 1$ atm Argon), on the silicon face of SiC [11]. The higher temperature (cf. 1250 ^{o}C in [7]) allow better crystallization of graphene and high pressures minimize the creation of defects on the substrate. This method reproducibly results in high-quality, large-area, single layer graphene, as confirmed by ARPES [11] and magnetotransport measurements [12, 13]; the results using similar growth techniques were confirmed by other groups thereafter [14–16].

Contributions and Scope

This thesis describes the use of magnetotransport as a tool to characterize graphene grown epitaxially on the silicon face of silicon carbide (SiC/G). Additionally, it presents the first application where graphene outperforms conventional semiconductors.

Chapter 2 introduces some concepts related to electron transport and graphene that might be useful throughout the discussion. It includes magnetotransport in the classic and quantum limits, and how this is modified for the case of graphene.

Chapter 3 describes the experimental techniques used to perform magnetotransport measurements on monolayer graphene; microfabrication of ohmic contacts and precision measurement techniques are described.

The growth of monolayer graphene on SiC and its identification through magnetotransport measurements is presented in Chapter 4 (appended papers **I** and **II**). Our observation of half-integer quantum Hall effect on graphene grown epitaxially on SiC for the first time confirmed the high temperature, high pressure growth as a reliable method to produce large-area, high-quality, monolayer graphene on SiC. Chapter 5 describes how to control and preserve the carrier concentration of the graphene monolayer, particularly useful for complete characterization and reproducible measurements (paper **III**).

A detailed analysis of electron transport in epitaxial graphene through quantum-mechanical effects is presented in Chapter 6 (paper **IV**). A study of weak localization allowed to identify the scattering mechanisms that degrade carrier mobility

[1] The samples studied in this work were kindly provided by this group.

in this material. It was found that the effect of electron scattering (believed to be weak in graphene) and localized magnetic impurities (from vacancies in the graphene crystal or impurities introduced during fabrication) are relevant.

Finally, Chapter 7 presents the application of graphene on SiC to redefine the unit of electrical resistance, the Ohm (Ω), by using the half-integer quantum Hall effect (paper **V**). The result is that due to the nature of the quantum Hall effect in this material, the measurements are more accurate and can potentially be more technically simple in terms of device fabrication and working temperature. The accuracy of the graphene standard is an order of magnitude better than GaAs heterostructures, currently used for these purposes.

Chapter 2

Concepts

2.1 Magnetotransport in 2D semiconductors

A simple but reasonably accurate description of electron transport is provided by the Drude model, which applies the kinetic theory of gases to the motion of electrons in solids. Electrons are treated as independent particles that respond to external forces by accelerating and travelling a distance λ, the mean free path, until they lose their momentum when experiencing collision with the ions in the lattice.

In the context of magnetotransport, the external forces acting on electrons are the electric and magnetic fields; electrons accelerate under the action of the electric fields and as they propagate they experience collisions at a rate τ^{-1}, and also interact with the external magnetic field. Once equilibrium is reached, electrons move with an average (drift) velocity v, which is found using Newton's equation:

$$\frac{d\vec{v}}{dt} = -\frac{e}{m^*}(\vec{E} + \vec{v} \times \vec{B}) - \frac{\vec{v}}{\tau} = 0 \tag{2.1}$$

with e the electron charge, m^* the effective mass of electrons, and the relaxation time $\tau = v/\lambda$. Using the fact that the electron current density J is related to the drift velocity v as $J = env$, with n the electron density, eq. 2.1 can be written in two dimensions as:

$$E = \rho J = \begin{pmatrix} \rho_{xx} & \rho_{xy} \\ \rho_{yx} & \rho_{yy} \end{pmatrix} J = \sigma_0^{-1} \begin{pmatrix} 1 & -\omega_c\tau \\ \omega_c\tau & 1 \end{pmatrix} J \tag{2.2}$$

with $\sigma_0 = ne^2\tau/m^*$ the Drude conductivity and $\omega_c = eB/m^*$ the cyclotron frequency. In the absence of magnetic field ($\omega_c = 0$), equation 2.2 reduces to Ohm's Law, $E = \sigma_0^{-1} J$.

2.1.1 Hall effect

When electrons propagate under crossed electric and magnetic fields (Figure 2.1a), the Lorentz force deflect their trajectories and accumulates them at the edges of the sample, giving rise to a potential build up in the y direction (V_y), the Hall voltage. From eq. 2.2 the measured transversal resistance[1] is:

$$\rho_{xy} = -\frac{V_{xy}}{i_{xx}} = \frac{-\omega_c\tau}{\sigma_0} = -\frac{B}{ne} \tag{2.3}$$

The constant of proportionality $1/ne$ is called the *Hall* coefficient. The magnitude and sign of the transversal resistance ρ_{xy} can be used as a tool to characterize conducting materials in terms of carrier type (electrons or holes) and density n (per unit area).

2.1.2 High magnetic fields

From classical considerations, in the Drude model the transversal resistance ρ_{xy} depends linearly on the externally applied magnetic field B (eq.2.3), while the longitudinal resistance ρ_{xx} is a constant.

For high mobility two-dimensional systems at low temperatures and strong magnetic fields this is not the case. Oscillations in $\rho_{xx}(B)$ and steps in $\rho_{xy}(B)$ are observed; the former are called Shubnikov-De Haas oscillations, and the later is the quantum Hall effect [17]. Both phenomena are the consequence of the

[1] For a two-dimensional sample with length L and width W, the 2D resistivity is defined as $\rho_{2D} = \rho/t$, with t the (infinitesimal) thickness of the sample. ρ_{2D} has the same dimensions as the 3D resistance (Ω)- In order to avoid confusion, the units of ρ_{2D} are most of the times explicitly written as $\Omega/(L/W) = \Omega$/square. Sometimes, however, the words *resistance* and *resistivity* for two-dimensional samples are used indistinctly.

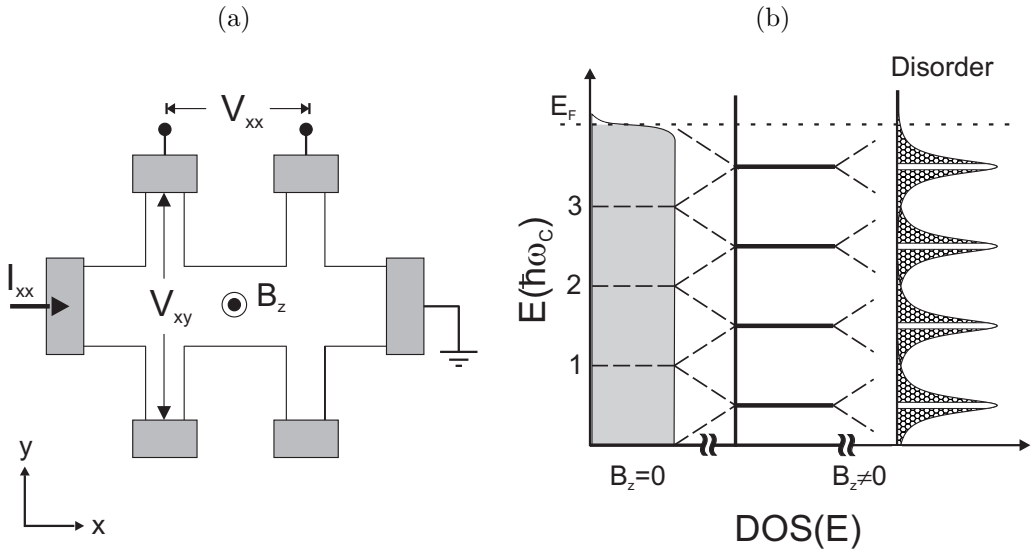

Figure 2.1: (a) Magnetotransport measurements in a Hall bar and the resistivity tensor (eq.2.2) enable the electrical characterization of a material in terms of carrier type (electrons or holes), concentration and mobility. The *sheet* (2D) resistivity is $\rho_{xx} = (V_{xx}/I_{xx})(W/L)$ and the *Hall* coefficient $R_H = V_{xy}/(BI_{xx})$. The carrier mobility can be found experimentally as $\mu = R_H/\rho_{xx} \times 10^4$ in units $\mathrm{cm^2V^{-1}s^{-1}}$. (b) In two-dimensional systems at low temperatures and high magnetic fields, quantization of cyclotron motion lead to formation of Landau levels (LL) in the density of states (DOS). In theory the levels, spaced by $\hbar\omega_c$, are highly degenerate delta functions, but in real samples the presence of disorder broadens the levels.

formation of Landau levels (LL) in the density of states (Figure 2.1b) due to quantization of the electron cyclotron motion: the cyclotron orbit has to fit an integer number times the electron wavelength. For this effect to be experimentally observable, an electron should be able to complete a few orbits before its momentum is relaxed due to scattering, that is,

$$\omega_c^{-1} \ll \tau \tag{2.4}$$

recalling that $\omega_c = eB/m^*$ and the mobility $\mu = e\tau/m$, condition (2.4) can be rewritten as $B \gg \mu^{-1}$. Thus, quantum effects can be observed with $B = 1$ Tesla if the mobility of the sample is around $\mu = 10,000\ \mathrm{cm^2V^{-1}s^{-1}}$. Formally, LL are

the different energy levels obtained by solving the Schrödinger equation for free electrons in the presence of a magnetic field. The problem reduces to that of a harmonic oscillator shifted by the magnetic length [18]:

$$\ell_B = \sqrt{\frac{\hbar}{eB}} \tag{2.5}$$

with eigenvalues given by:

$$E_N = \hbar\omega_c(N + \frac{1}{2}) \tag{2.6}$$

with N an integer, zero included. In theory, each LL in a clean system is responsible for a delta function in the density of states. However, the presence of disorder in real samples broadens the levels (Figure 2.1b). In a system with initial electron density n, the amount of filled Landau levels (so-called filling factor) can be found by dividing the density of electrons in the system by the number of localized electrons, n_{LL}.

$$\nu = n/n_{LL} \tag{2.7}$$

Noticing that each localized electron, undergoing cyclotron motion, encloses a quantum of magnetic flux $\Phi_0 = h/e$, the amount of localized electrons per unit area can be found by dividing the externally applied magnetic flux density by $\Phi_0 = h/e$

$$n_{LL} = eB/h \tag{2.8}$$

2.1.3 Integer quantum Hall effect (QHE)

At low magnetic fields the transversal resistance ρ_{xy} depends linearly on the applied magnetic field, but in the quantum Hall regime ρ_{xy} displays plateaux at values $h/\nu e^2$, where ν takes an integer value different from zero, and simultaneously $\rho_{xx} = 0$ (Figure 2.2a).

The quantization of the Hall effect can be understood by considering that the density of states breaks into (discrete) Landau levels; when a LL is full, the Fermi level must lie in a gap between occupied levels and the filling fact ν in eq. 2.7 must be an integer. If we substitute the discrete density of states resulting from the formation of LL, n=νn$_{LL}$ (eq. 2.7) into the dependence $\rho_{xy}(B)$ for the classic

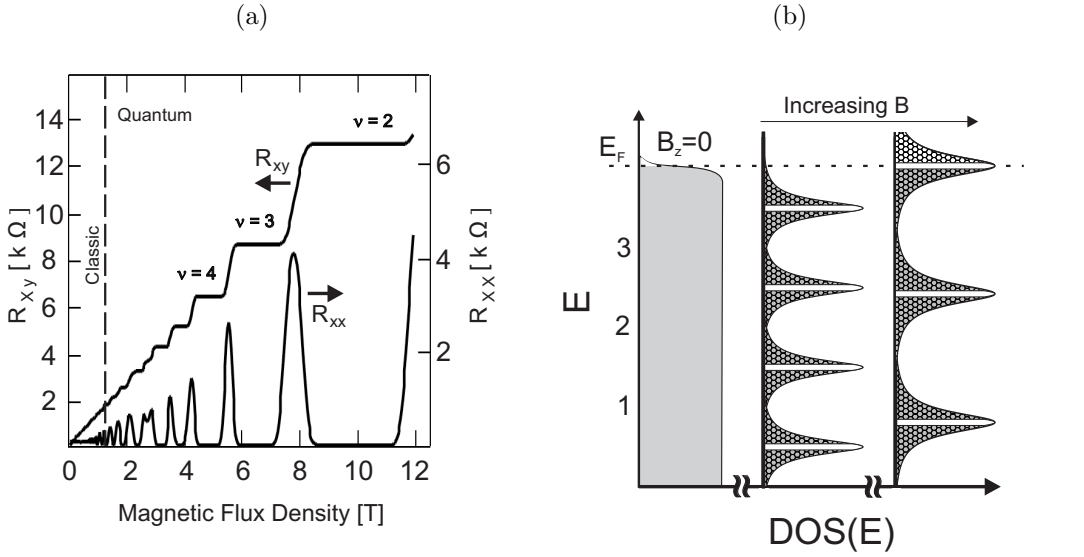

Figure 2.2: (a) Classic (quantum) Hall effect at low (high) magnetic fields in conventional, semiconductor-based, two-dimensional systems. (b) In the absence of electrostatic gate the electron concentration remains constant and the quantum Hall plateaux are observed by increasing the magnetic field B, whenever the Fermi energy lies in between the the center of Landau levels.

Hall effect (eq. 2.3), we find that ρ_{xy} is quantized as:

$$\rho_{xy} = \frac{B}{en} = \frac{B}{e\nu n_{LL}} = \frac{B}{e\nu(eB/h)} = \frac{h}{\nu e^2} \tag{2.9}$$

A common interpretation for QHE is in the picture of extended states, carrying current without dissipation (zero resistance) along the edges of the sample, and localized states undergoing cyclotron motion in the bulk. The origin of zero longitudinal resistance ρ_{xx} is that extended states propagating in one direction of the sample are spatially separated from those carrying current in opposite direction, suppressing in this way backscattering.

Experimentally, quantum Hall plateaux can be observed by: a) fixing the magnetic field and varying the Fermi level of the sample with e.g. an electrostatic gate or b) fixing the Fermi level (fixed carrier concentration) and varying the magnetic field B (Figure 2.2b). In any case, maxima in ρ_{xx} is observed every time the Fermi level crosses the center of a LL; plateaux in ρ_{xy} and vanishing ρ_{xx}

are observed whenever the Fermi level lies in between the center of LL, pinned by localized states. It is in fact due to localized states that the electrochemical potential can change continuously with magnetic field.

2.1.4 Quantum interference

In real electrical conductors, excessive elastic scattering can lead to the diffusive regime. In this scenario, the classical diffusive current due to electrons is $J_d = -D\nabla^2 n$, where D is the diffusion coefficient ($D = v_F l/2$ in 2D) and n is the electron density. In the quantum (diffusive) limit, corrections to the classic Drude[1] conductivity σ_0 arise due to interference of wave-like carriers, namely (universal) fluctuations in the conductance (UCF) and the weak localization of electrons (WL); only the latter is of interest to this thesis.

Weak Localization correction to Drude conductivity

At low temperatures, WL manifests itself as an increase of the electrical resistance (decrease in conductance) of a 2D system that can be suppressed by applying a perpendicular magnetic field. WL can be explained by considering the conductivity of a medium is proportional to the probability of electrons to propagate through it. The total transmission probability is obtained by squaring the sum of the *quantum-mechanical amplitudes* of all possible paths [19, 20], denoted as $A_i = a_i e^{i\phi_i}$:

$$P_{Tot} =\mid A_{Tot} \mid^2 =\mid \Sigma_i A_i \mid^2 = \Sigma_i P_i + 2Re\Sigma_{ij} A_i^* A_j \tag{2.10}$$

where the term $\Sigma_i P_i = \Sigma_i \mid a_i^2 \mid$ represents the classical probability and the term $2Re\Sigma_{ij} A_i^* A_j$ is the (quantum-mechanical) interference. For random paths i, j there is no special phase relation between A_i and A_j , and the interference term averages to zero. Nevertheless, there are certain paths where $A_i = A_j$ and the interference term is non-zero, e.g. self-crossing trajectories (related by time-reversal symmetry, $t \to -t$) (Figure 2.3a), such that the overall probability P_{Tot}

[1] In the Drude model, scattering process enter through the momentum relaxation rate, and normally resistance decreases with decreasing temperature, $\tau^{-1} = \tau^{-1}_{impurities} + \tau^{-1}_{electron-electron} + \tau^{-1}_{phonon} = A + BT^2 + BT^5$

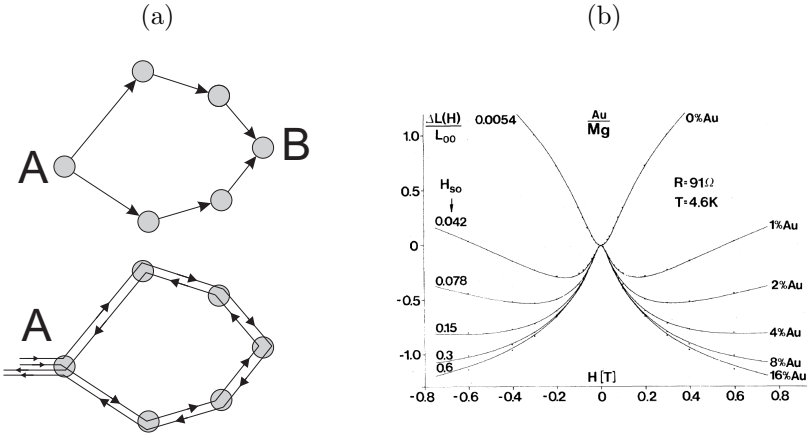

Figure 2.3: (a) Quantum interference effects average to zero for trajectories of the type $A \to B$; weak localization corrections are relevant for time-reversal symmetric trajectories (e.g. closed-loops $A \to A$) in which the phases of two counter propagating electrons ϕ_i and ϕ_j are equal. In these trajectories, the probability of backscattering is enhanced (duplicated) since $P_T = \Sigma_i P_i + \Sigma_i a_i a_j e^{(\phi_i - \phi_j)} = 2\Sigma_i P_i$ (eq.2.10). (b) Experimental demonstration of the transition from weak localization (WL) to antilocalization (WAL) in thin films of magnesium. The positive to negative magnetoconductance was achieved by introducing Au impurities on Mg thin films, which cause spin-orbit scattering [21].

has an additional contribution from the interference term. The fact that self-crossing paths have greater return probability indicates enhanced backscattering and therefore lower conductivity due to interference effects.

A perpendicular magnetic field breaks time reversal symmetry by adding different phases to counter propagating electrons, $\phi_i \neq \phi_j$, and this suppress interference effects. Thus, the WL manifests as a peak at $B = 0$ in the magnetoresistance $\rho_{xx}(B)$ (dip in magnetoconductance $\sigma_{xx}(B)$) and its amplitude and width are used to characterize the nature of carriers and disorder. The longer the waves can stay coherent, the bigger the area encircled by the loop can be (Figure 2.3a) and the smaller the magnetic flux density (B) needed to suppress WL corrections; a sharper WL peak in ρ_{xx}(B=0) hence implies longer coherence lengths L_ϕ.

The type of scattering in the system can be distinguished by studying weak localization effects; scattering with spin-orbit coupling effects is particularly interesting because it can lead to a positive magnetoresistance (negative magne-

toconductance): as the perpendicular magnetic field is applied, the resistance (conductance) will increase (decrease), the so-called weak anti localization effect (WAL). Understanding this phenomenon requires taking into account the spin degree of freedom; in the semi-classical picture, the spin of electrons is rotated by the impurities as it scatters, so when counter propagating electrons meet at the starting point (e.g. at A in figure 2.3a) they are in anti-phase, suppressing in this way any interference and therefore backscattering. In general, the study of WL/WAL and its temperature dependence provides information about inelastic scattering mechanisms leading to decoherence, such as magnetic impurities or interactions between electrons.

2.2 Graphene

The description of magnetotransport provided so far is valid for *conventional* two-dimensional systems, that is, those formed by confining electrons at interfaces of semiconductors (e.g. Si/SiO_2 or AlGaAs/GaAs). Graphene, on the other hand, is a true two-dimensional crystal with a peculiar electronic structure: a linear E(k) dispersion compared to parabolic, in conventional 2D systems. The following sections present an overview of graphene and the implications of its electronic structure for magnetotransport.

2.2.1 Crystal and electronic Structure

Graphene owes its two-dimensional nature to sp^2 hybridization of carbon atoms. Prior bonding, the ground state electronic configuration of a carbon atom is modified due to electron promotion[1], and the frontier orbitals available for bonding are linear combinations of two p orbitals ($2p_x$ and $2p_y$) and one s orbital ($2s$) in each carbon atom. The resulting molecular orbitals consist of in-plane localized σ bonds, between carbon atoms, and out-of-plane π electrons delocalized over the entire crystal. Each carbon atom has three nearest neighbors, separated by $\sim 120^o$ giving graphene its peculiar honeycomb structure.

[1] In a simplistic way, one electron from the 2s orbital occupies the empty $2p_z$ prior chemical bonding: $1s^2\ 2s^2\ 2p_x^1\ 2p_y^1 \rightarrow 1s^2\ 2s^1\ 2p_x^1\ 2p_y^1\ 2p_z^1$

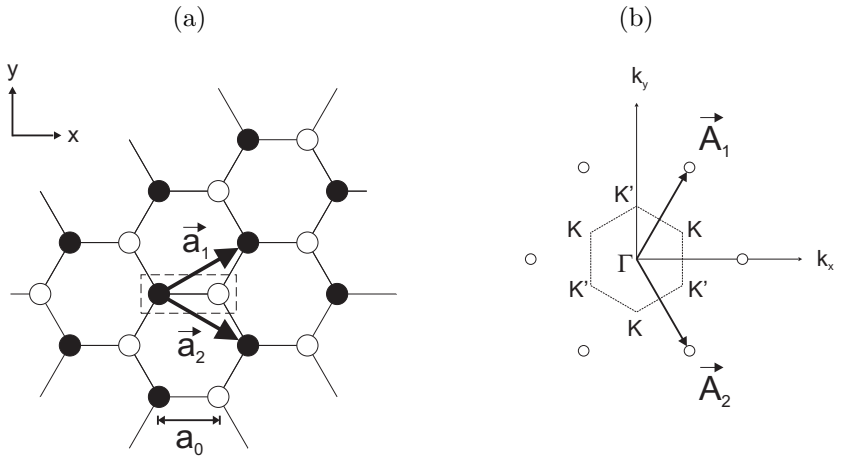

Figure 2.4: (a) Graphene honeycomb structure (direct space); the unit cell contains two carbon atoms separated by $a_0 = 1.42\mathring{A}$. (b) Reciprocal lattice showing the first Brillouin zone (FBZ); six points at the corner of the FBZ fall into two groups of equivalent points, denoted as K and K'.

The graphene lattice is described by a unit cell that comprises two atoms, A and B, periodically arranged in a triangular lattice (Figure 2.4a). In real space, the primitive vectors are given by $\vec{a}_1 = \hat{x}a + \hat{y}b$ and $\vec{a}_2 = \hat{x}a - \hat{y}b$, $a \equiv 3a_0/2$, $b \equiv \sqrt{3}a_0/2$ and the distance between nearest neighbors $a_0 = 1.42$ Å. The reciprocal lattice is constructed as $\vec{K} = M\vec{A}_1 + N\vec{A}_2$, where (M,N) are integers and the primitive vector in the reciprocal lattice $\vec{A}_1$ and $\vec{A}_2$ are determined from the condition $a_i \cdot A_j = 2\pi\delta_{ij}$: $\vec{A}_1 = \hat{x}(\pi/a) + \hat{y}(\pi/b)$ and $\vec{A}_2 = \hat{x}(\pi/a) - \hat{y}(\pi/b)$ (Figure 2.4b).

Since graphene is a covalent solid, a good approximation of its electronic band structure can be found using a tight-binding description [3]. In graphene two basis functions are used per unit cell, one (p_z) orbital per carbon atom; this is justified by sp^2 bonding, in which the σ bonds, localized in the graphene plane, are decoupled from the p_z orbitals, delocalized over the entire crystal. Generalization from the unit cell to the entire solid is achieved by using Bloch function as ansatz. The band structure is described by [22]:

$$E = \pm t\sqrt{1 + 4\cos(k_y b)\cos(k_x a) + 4\cos^2(k_y b)} \tag{2.11}$$

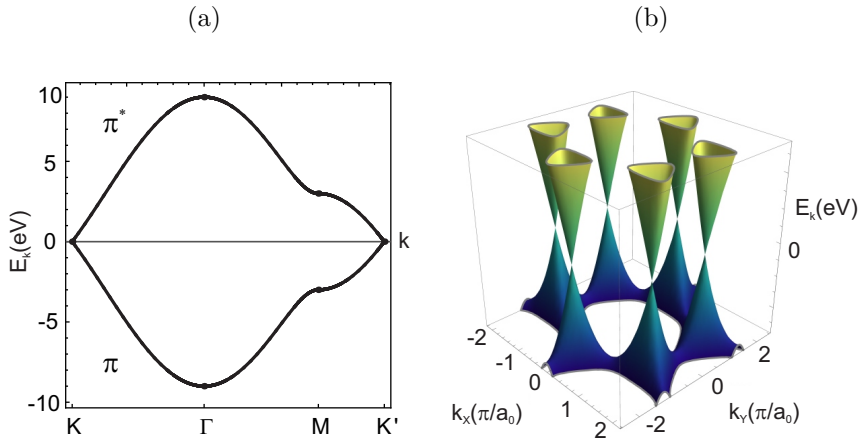

Figure 2.5: (a) Calculation of graphene bandstructure using a hoping parameter $t = -3$ eV; the bands are shown along the main crystallographic directions, including the K and K' points. (b) Detail of the energy dispersion around $E = 0$ (Dirac points). The Dirac cones are distorted at high energies due to corrections from next-nearest-neighbor hoping (*trigonal warping*).

The two bands, a consequence of having two basis functions per unit cell, are symmetric about $E = 0$. In neutral graphene the Fermi level lies at $E = 0$, and all the states with $E < 0$ are filled while those with $E > 0$ are empty (Figure 2.5). In reciprocal space, the location of the charge-neutrality point ($E = 0$) is found by setting eq.2.11 $= 0$; with $k_x a = 0$, the condition $E = 0$ is satisfied at the six corners of the first Brillouin zone, shown in figure 2.4b. The 6 corners fall in two groups of three equivalent points, differing only by a reciprocal lattice vector. These two groups represent then two non-equivalent points, named for crystallographic convention K and K'.

Remarkably, a rather simple Hückel tight-binding model provides an accurate description of graphene, as confirmed by angle-resolved photo-electron spectroscopy (ARPES), a technique that can directly probe the band structure of a crystal [23]. Graphene is thus a zero band gap semi-metal, with the Fermi level located at the intersections between the valence and conduction (π and π^*) bands, which are located at the K and K' points in k-space.

2.2.2 Low-energy spectrum

The results from the tight-binding model are particularly interesting close to the K and K' points in reciprocal space, where the energy dispersion $E \propto k$, in contrast to $E \propto k^2$ as in conventional electrical semiconductors. Around these K, K' points, the energy dispersion of carriers is similar to that of ultra-relativistic particles with zero rest mass m_0, $E(\vec{k}) = \sqrt{m_0^2c^4 + c^2\hbar^2k^2} = c\hbar k$; under these conditions the Schrödinger equation for Bloch electrons reduces to the 2D Dirac equation. The Dirac equations is thus used to describe the behaviour of carriers, massless Dirac Fermions, around the K, K' points, which are also called for this reason *Dirac points*.

By taking the K(K') point as reference and defining a vector momentum relative to this point as $q = k - K$ ($q' = k - K'$), the eigenfunctions in momentum representation for the pseudo-relativistic carriers are:

K	K'
$\psi_{+,K}(q) = \frac{1}{\sqrt{2}} \begin{pmatrix} e^{-i\theta_k/2} \\ e^{i\theta_k/2} \end{pmatrix}$	$\begin{pmatrix} e^{i\theta_k/2} \\ e^{-i\theta_k/2} \end{pmatrix} \frac{1}{\sqrt{2}} = \psi_{+,K'}(q')$
$\psi_{-,K}(q) = \frac{1}{\sqrt{2}} \begin{pmatrix} e^{-i\theta_k/2} \\ -e^{i\theta_k/2} \end{pmatrix}$	$\begin{pmatrix} e^{i\theta_k/2} \\ -e^{-i\theta_k/2} \end{pmatrix} \frac{1}{\sqrt{2}} = \psi_{-,K'}(q')$

(2.12)

where the $+/-$ signs correspond to energies of the π^* and π bands, respectively (Figure 2.5a). The wave functions (2.12) are described as a two component spinor, a linear combination of excitations arising from the A and B sublattice (π and π^* bands). The *pseudo-spin*, quantified by the angle θ_k, is in fact related to the vector momentum of the carriers,

$$\theta_k = \arctan\left(\frac{q_x}{q_y}\right) \tag{2.13}$$

Since θ_k is a function of momentum, it follows that the wavefunctions (2.12) at K and K' are related by time-reversal symmetry ($t \to -t$). Another consequence

of the pseudo-spin being associated to the vector momentum q, is that when carriers move in a full circle the wavefunction changes sign (or equivalently, it accumulates an effective phase $e^{\pm i\pi}$). Taking as an example one of the components of $\Psi_{+,K}(k)$, a change of $360^o = 2\pi$ results in $e^{-i(\theta_K+2\pi)/2} = e^{-i\pi}e^{-i\theta_k/2} = -e^{-i\theta_k/2}$. This is also called *geometric* or *Berry* phase, and it has interesting implications whenever electrons in graphene move along closed trajectories, as for cyclotron motion at high magnetic fields or self-crossing paths in quantum diffusive regime at low magnetic fields (section 2.1.4).

In summary, particles close to the Fermi level in neutral graphene, the K, K' or Dirac points, display an energy spectrum that depends linearly on momentum (as for ultra-relativistic particles); this is a consequence of the fact that the wavefunctions of the carriers are effectively eigenfunctions of the 2D Dirac equation. Carries are modelled as if they had zero rest mass and possessed a spin; this latter is in fact related to the vector momentum of carriers so rotation of 2π changes the sign of the wavefunction (Berry phase).

2.3 Magnetotransport in graphene

The motion of Dirac Fermions in graphene can be described within the Drude model for low magnetic fields. Close to the Dirac point the linear spectrum $E(k)$ implies zero rest mass; away from the Dirac point however, it has been observed experimentally through cyclotron motion experiments that the mass of carriers in graphene obeys [2]:

$$m_G^* = \frac{\sqrt{\pi}}{v_F}\sqrt{n} \tag{2.14}$$

with Fermi velocity $v_F \approx 10^6 m/s$. For magnetic fields large enough so that the Dirac Fermions undergo cyclotron motion, the Berry phase accumulated by carriers when completing a full turn around the K, K' points manifests in novel and unique magnetotransport features, as described below.

2.3.1 Half-Integer quantum Hall effect

In graphene, the circular motion of carriers is anomalous in a sense that when carriers complete an orbit (2π) they "are not the same"; additionally, due to the lack of mass, the expression for the cyclotron frequency for Dirac Fermions is modified [2, 24]:

$$\omega_c = \sqrt{2}\frac{v_F}{\ell_B} = v_F\sqrt{\frac{2eB}{h}} \tag{2.15}$$

The facts that carriers can be modelled as having no mass and that they accumulate an effective phase of π upon completing a full turn have profound implications in the Landau level spectrum of monolayer graphene (Figure 2.6a). In comparison to the case of carriers with finite mass in conventional 2D systems, LL for chiral carriers in graphene are found by solving the Dirac equation in the presence of electric and magnetic field. The LL spectrum is given by [2, 24, 25]:

$$E_{LL-Gr} = \pm\hbar\omega_c\sqrt{N} = v_F\sqrt{2\hbar eBN} \tag{2.16}$$

with N an integer number including zero. The main differences with conventional 2D systems (eq.2.6) are:

- The energy spacing depends on the magnetic field as $\Delta E_{LL} \propto \sqrt{B}$, instead of $\Delta E_{LL} \propto B$ as in conventional 2D systems.
- Each Landau level can take twice as many electrons as in conventional 2D systems. This four-fold degeneracy is due to spin-up/spin-down (as in conventional 2D systems), and valley degeneracy, K and K' (particular to monolayer graphene).
- There exists a LL at $E = 0$, "shared" by the two valleys K and K'. As a consequence, this particular zero-energy LL is only two-fold degenerate (spin).

This anomalous Landau Level spectrum manifests in a peculiar sequence of plateaux in ρ_{xy} in the quantum Hall regime, the so-called half-integer quantum Hall effect (Figure 2.6b). This can be understood by recalling the case of conventional 2D systems, in which each (spin degenerate) Landau Level can allocate

$2eB/h$ electrons (per unit area) (eq. 2.8). In addition to spin degeneracy, in graphene there exist an additional double degeneracy due to two valleys, K and K'. Thus, the electron density n_G corresponding to N filled LL in graphene, when the Fermi level lies in a gap between occupied levels, is

$$n_G = N\frac{2eB}{h}|_K + N\frac{2eB}{h}|_{K'} + \frac{2eB}{h}|_{E=0} = \frac{4eB}{h}(N + 1/2) \tag{2.17}$$

By substituting the discretized density of states n_G (eq.2.17) into the formula for the conventional Hall effect (eq. 2.3), we arrive at the sequence of plateaux for the half-integer Quantum Hall effect:

$$\rho_{xy} = \frac{B}{en_G} = \frac{B}{e[4eB(N + 1/2)/h]} = \frac{h}{4e^2(N + 1/2)} \tag{2.18}$$

As discussed before for the integer QHE, plateaux in ρ_{xy} are observed every time the Fermi level lies in between the center of LL. In graphene each Landau level contributes thus effectively with four extended states (spin and valley degeneracy), with the exception of the zero-energy Landau level, which is shared by the two valleys and contributes only with two extended states (spin degeneracy). Half-integer quantum Hall effect is the fingerprint of monolayer graphene, and can be used experimentally to prove that electronic transport occurs through a single graphene layer.

2.3.2 Weak (anti) localization in graphene

Weak anti-localization (WAL) is expected in graphene as a consequence of the extra Berry phase accumulated by electrons moving around a closed loop; after traversing the closed loop in opposite directions, counter-propagating electrons meet in anti phase and this leads to a suppression of interference effects. Despite being natural for chiral carriers to display WAL, (real) spin-orbit coupling can also result in WAL as in the case of conventional conductors.

Weak localization (WL) in graphene is nevertheless possible if elastic scattering is introduced; this is the main difference with conventional 2D systems, where weak localization is only sensitive to inelastic scattering. Elastic scattering can change the momentum of carriers, which in turn changes the phase of the wave

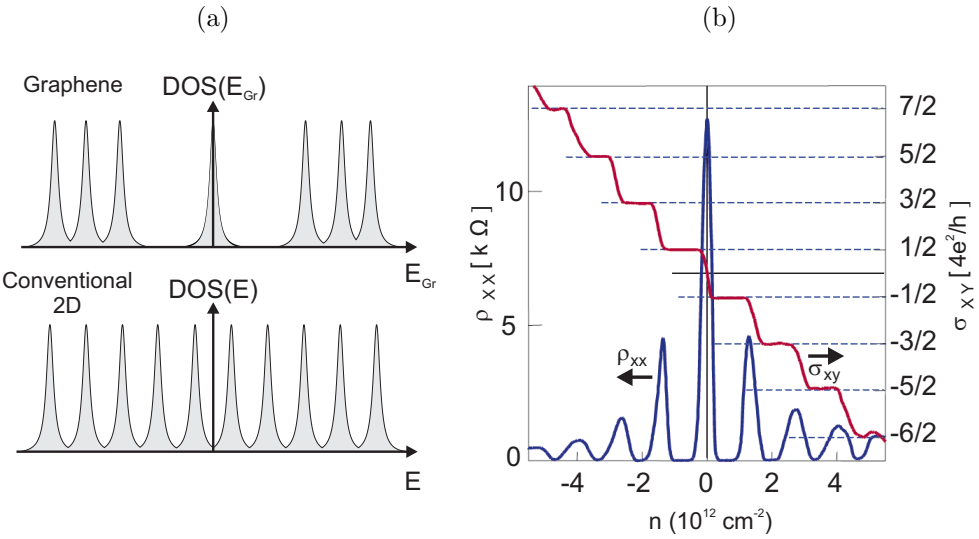

Figure 2.6: (a) The sequence on Landau levels in graphene is unique; the energy spacing depends on the magnetic field as $\Delta E_{LL} \propto \sqrt{B}$, instead of $\Delta E_{LL} \propto B$ as in conventional 2D systems and there exists a LL at E=0, "shared" by the two valleys K and K'. (b) Half-integer quantum Hall effect measured in exfoliated graphene flakes by fixing the magnetic field to $B = 12$ T and varying the carrier concentration with a bottom electrostatic gate (adapted from [26]).

function, the pseudo-spin (eq.2.13). This has the effect of carriers apparently changing of valley from $K \leftrightarrow K'$, or changing the phase θ_K of the A-B sublattice parts within the same valley.

The overall result is that both WL and WAL is possible in graphene; the sign of the magnetoresistance depends on the type (and intensity) of scattering in the systems. Apart from inelastic scattering (decoherence), the theory of weak localization for graphene [27–29] takes into account mainly three characteristic scattering processes:

- **Intervalley scattering.** Caused by very short-range potentials (at the scale of the lattice constant). It can be originated by e.g. some adatoms, adsorbed hydrocarbons, vacancies or edges of the sample. Intervalley scattering restores WL because it allows the counter propagating electrons to occupy different valleys. Since the electrons in the two valleys are related by time reversal symmetry, the phases acquired by two electrons, one in

the K valley and its time-reversed version at K' are equal, allowing for constructive interference.

- **Intravalley scattering.** Arising from long-range scattering potentials, such as ripples, dislocations, charged impurities or topological defects. This type of scattering randomizes the phase within a valley suppressing interference effects from the same valley and thus localization effects.

- **Trigonal warping.** The fact that the energy dispersion $E(k)$ for carriers in graphene is not linear to second order can introduce corrections, specially if the Fermi level is far away from the Dirac point (Figure 2.5b). It allows for some amount of backscattering within the same valley.

The characteristic scattering times encompassed by the theory are the decoherence (τ_ϕ), intervalley scattering length (τ_i) and the combined effect of trigonal warping and intravalley scattering (τ_*). At $B = 0$, the temperature dependent WL correction to the resistivity of graphene reads

$$\Delta\rho(B=0,T) = \frac{e^2\rho^2}{\pi h}\left[\ln\left(1+2\frac{\tau_\phi}{\tau_i}\right) - 2\ln\left(\frac{\tau_\phi/\tau}{1+\tau_i/\tau_*}\right)\right] \tag{2.19}$$

where τ is the relaxation time and the scattering times $\tau_{\phi,i,*}$ are found by fitting the measured $\rho_{xx}(B,\bar{T})$ to (2.20):

$$\frac{\Delta\rho(B,\bar{T})}{\rho^2} = -\frac{e^2}{\pi h}\left[F\left(\frac{B}{B_\phi}\right) - F\left(\frac{B}{B_\phi+2B_i}\right) - 2F\left(\frac{B}{B_\phi+B_*}\right)\right] \tag{2.20}$$

where $F(z) = ln(z) + \Psi(\frac{1}{2}+\frac{1}{z})$, Ψ is the digamma function and the characteristic fields are $B_{\phi,i,*} = \frac{\hbar}{4De}\tau^{-1}_{\phi,i,*}$

The interplay between the different scattering rates causes a transition from WAL to WL in graphene. This has been experimentally verified for graphene flakes by tuning $L_{\phi,i,*}$ by: a) increasing temperature to reduce the dephasing length and b) increasing the intervalley scattering length by decreasing carrier density(After [30]).

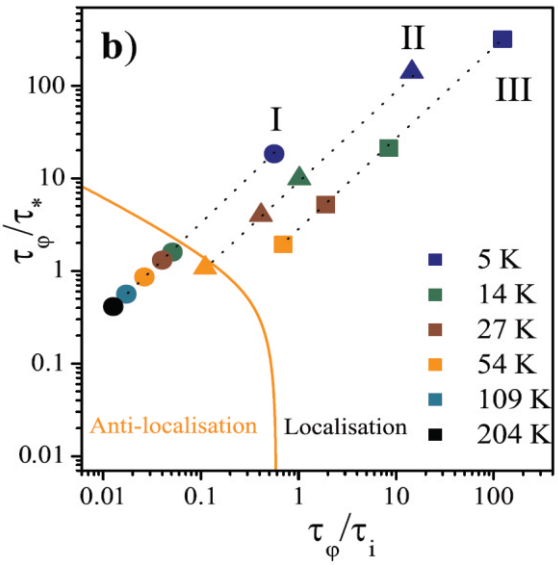

Figure 2.7: The $WL \leftrightarrow WAL$ transition has been observed experimentally in graphene flakes. Positive or negative magnetoresistance is possible by adjusting the characteristic times τ_ϕ and τ_i. This was achieved by changing the temperature (in order to change τ_ϕ) and also the carrier concentration in the sample (to modify τ_i) (After [30]).

Chapter 3

Experimental Techniques

The study of electron motion through an electrically conducting system in the presence of magnetic field -magnetotransport-, can be used as a powerful electronic characterization tool. At room temperature, Hall effect data obtained at low magnetic fields is used to extract electron density and mobility while at low temperatures ($T = 4$ K) quantum-mechanical corrections to the electrical resistance can be used to understand the nature of electron scattering processes. At high magnetic fields, the dimensionality of the systems can be unveiled through quantum phenomena. In particular for graphene, the position of plateaus in the quantum Hall regime can be used to distinguish the number of layers that contribute to electron transport.

This chapter describes the experimental techniques used to characterize epitaxial graphene grown on the silicon face of SiC through magnetotransport measurements. The chapter starts with the fabrication of graphene micro structures, including the formation of ohmic contacts, followed by a description of high-precision electrical measurements required to measure quantum effects. Finally, an overview of metrological techniques used to develop a new standard of electrical resistance is given.

3.1 Microfabrication

Epitaxial graphene on SiC enables the use of traditional top-down, silicon-oriented techniques for fabrication of microdevices. We exploit this advantage for parallel fabrication of Hall bars on SiC substrates where monolayer graphene has been previously grown and characterized using Raman spectroscopy.

Fabrication of Hall bars includes three steps: 1) metallic anchors on SiC for electric contacts to graphene, 2) ohmic contacts to graphene 3) selective removal of graphene to define structures (Figure 3.1). All steps involve electron beam (e-beam) lithography; although lower accelerating voltages (50kV) are preferred, 100 kV have been also used without noticing any special difference for feature sizes $\gtrsim 10$ μm. Our process is limited to the use of certain resists and solvents which showed not to degrade the electronic performance of the devices. For further details see Appendix A

1. **Metallic Anchors.** Metallic contacts directly deposited on graphene are prone to lift-off and additionally bonding, attaching wires for electrical measurements, was in most of the cases not possible. For this reason, metallic anchors are fabricated directly on SiC by first removing graphene using plasma etching after e-beam exposure and development and second, e-beam evaporation of titanium (adhesion layer) and gold. The process is completed by lifting- off in acetone.

2. **Ohmic contacts.** Electrical contacts are defined on top of both metallic anchors and graphene. Fabrication is the same as for the anchors except for: a) avoid the removal of graphene and b) add an extra overlap area, needed to contacts graphene. This process produces ohmic contacts as low as ~ 1 Ω [13].

3. **Hall bar definition.** The final step is to carve out the desired pattern, in this case Hall bars using e-beam lithography with positive resist followed by oxygen plasma etching.

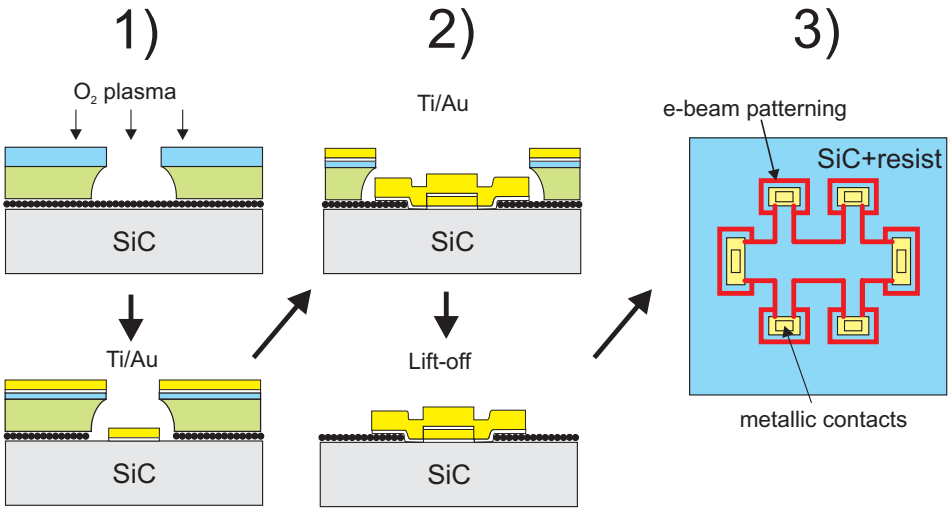

Figure 3.1: Microfabrication process based on electron beam (e-beam) lithography. 1) Metallic anchors are fabricated by evaporating Ti/Au (5/70 nm); 2) ohmic contacts are fabricated by depositing Ti/Au (5/100 nm) onto both, the anchors and graphene; 3) the last step consists in "carving out" the desired geometry (Hall bars) using e-beam exposure and removal of graphene with O_2 plasma.

3.2 Magnetotransport

A typical silicon carbide chip with graphene we use in our experiments is 7×7 mm^2. Initial characterization of the as-grown graphene in terms of sheet resistance, carrier concentration and mobility is performed at room temperature and low magnetic fields ($B \leq |1|$ T). For this step microfabrication is not necessary; instead, Van der Pauw measurements using indium contacts at the four corners of the chip are employed to provide a good approximation of the electronic properties of the sample. Typical outcome of these measurements is $\rho_{xx} \approx 1$ kΩ/square, $n \approx 1.2 \times 10^{12}$ cm^{-2} and $\mu \approx 3,000$ cm^{2}V^{-1}s^{-1}.

Hall bars allow one to probe smaller and therefore more homogeneous areas of graphene, which require finer characterization. The dimensions of the Hall bars, patterned as described in section 3.1, are in the range 1 μm to 50 μm in width and from 10 to 300 μm in length. After microfabrication, low temperature magnetotransport is used to confirm the single-layer nature of the sample. Four-probe (to exclude any effect of metallic contacts) DC measurements are performed in a

(helium) gas flow cryostat (Maglab Measurement systems, Oxford Instruments) at temperatures as low as T= 2 K and magnetic field ($B \leq |5|$ T).

3.3 Measuring Decoherence

Any measurement action on a system implies its perturbation. In particular for mesoscopic systems, if its equilibrium properties are to be probed, the perturbation has to be small compared to the energy scale of the system, otherwise the measurement backaction can lead to misleading results. In order to perform non-invasive measurements of quantum effects on SiC/G we focused on two aspects: 1) avoid overheating and 2) proper (electromagnetic) filtering.

Avoiding overheating

High voltage bias or current densities can drive the electronic system out of equilibrium due to e.g. Joule heating or by modifying the local density of states due to excessive electric fields. A condition which is sufficient (although not necessary, see Ref. [18]) to avoid overheating is to use a voltage bias less than $k_B T/e$, with k_B the Boltzmann constant, T being the base temperature and e the electron charge.

For measurements of decoherence at temperatures $T < 2$ K the amplitude of the voltage across the sample never exceed $k_B T/e$. As an example, for the lowest base temperature ($T = 25$ mK) in a dilution refrigerator, the current level of 50 pA was applied to a sample with $\rho_{xx} \approx 20$ kΩproduced an effective electron temperature of T=$(50 \times 10^{-12})(20 \times 10^3)(e/K_B) = \approx 12$ mK. Four-probe measurements, to exclude the effect of contacts, were carried out using lock-in demodulation at frequency $f = 17$ Hz.

For higher temperatures, $T \geq 2$ K four-probe DC measurements were performed in a (helium) gas-flow cryostat; current levels from 10 nA up to a 1μA showed no significant difference in terms of coherence; a current of 100 nA was used as a trade-off between signal-to-noise ratio and warming up the system. Current reversal[1] was used for all measurements to eliminate thermo-electric voltages.

[1]The resistance is measured at positive and negative currents i, $R = (R(+i) - R(-i))/2$

Filtering

Coupling a mesoscopic system to the macroscopic world through measurement leads can introduce electromagnetic noise (photons) strong enough to drive the system out of equilibrium. A photon with $f = 1$ GHz corresponds to a temperature $T = hf/K_B \approx 48$ mK; the overall effect of this photons (noise) is to heat up the electron systems beyond the base temperature of the cryostat.

Proper filtering to reduce high frequency noise can be achieved by using microwave cryogenic filters, based on the skin effect in metals [31, 32]. These filters are implemented by winding a wire and surrounding it by fine grain metallic powders, typically copper, bronze or stainless steel with size $\sim 20 - 50\mu$m in order to maximize area to volume ratio; the input and output are the ends of the wire. Since the skin effect occurs only at high frequency, powder filters display a poor performance at low-frequencies and are thus used in combination with other low pass filters . Attenuation of -120 dB at frequencies up to $f = 50$ GHz have been demonstrated with these [32].

In our measurement set-up, proper filtering allows electron temperatures as low as $T = 20$ mK, as confirmed by experiments of Macroscopic quantum tunnelling in Josephson junctions using escape rates from superconducting state into normal state as primary thermometer [33]. The dilution refrigerator contains two stages of filtering: a low pass at the $1K$ pot ($f_c = 100$ MHz) and a combination of thermocoax and copper powder filter ($f_c = 1$ GHz) at the mixing chamber.

3.4 Fits to weak localization theory

The correction to conductivity due to weak localization depends on three parameters, the characteristic scattering times τ_ϕ, τ_i and τ_*. These values are found by fitting our low-field, low-temperature magnetotransport measurements to the weak localization (WL) theory of graphene (eq. 2.20). The use of automated algorithms was not possible since our measurements could be fitted to a great extent by only two parameters, τ_ϕ and τ_i; local minima in the error function often produced erroneous results.

Instead, fits were performed in a semi-manual fashion. In a graphical user

interface[1] the experimental plot and the analytical fit were plotted simultaneously and the parameters τ_ϕ, τ_i and τ_* were manually adjusted to get a match (Figure 3.2). The maximum magnetic field for the validity of the fit was chosen by the conditions that the magnetic length ℓ_B should not exceed the mean free path, ℓ and no Shubnikov-de Hass oscillations were present.

An additional reference was provided by the error function:

$$E(\tau_\phi, \tau_i, \tau_*) = \Delta\rho_{xx,Theory}(\tau_\phi, \tau_i, \tau_*) - \Delta\rho_{xx,Measured} \tag{3.1}$$

which was minimized by adjusting the parameters iteratively. Eventually, a slightly different combination of parameters produced roughly the same error; these variations were used as error bars.

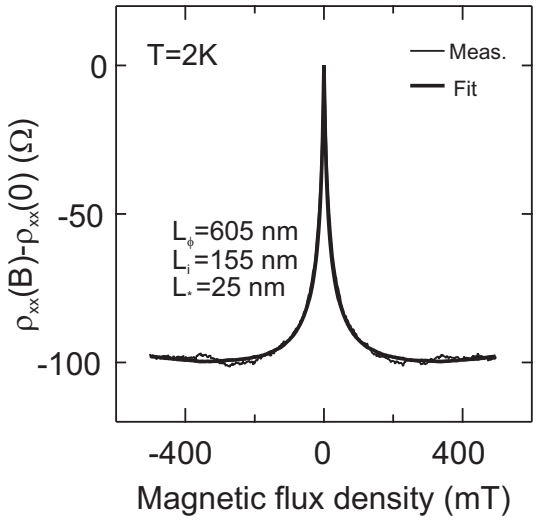

Figure 3.2: Fitting of experimental data of magnetotransport to the theory of weak localization in graphene. The experimental plot and the analytical fit were plotted simultaneously in a custom-made graphical user interface and the parameters τ_ϕ, τ_i and τ_* were manually adjusted to get a match.

[1] implemented with National Instruments Labview

3.5 Metrological techniques

The unit of electrical resistance, the Ohm (Ω), is nowadays defined using the Hall resistance of a two-dimensional system in the quantum Hall regime. The quantum Hall effect reduces the measurement of $R_K = h/e^2$ Ω, the ratio of two fundamental constants (the Planck constant h and the electron charge e), to a high-precision resistance measurement.[1]

The measurement and calibration of a resistor against R_K can be achieved with a current comparator bridge. In this set-up (Figure 3.3a), two resistances R_K and R_S are compared and for this purpose placed in different current loops. If the current flowing through both resistors is exactly the same, the calibration reduces to measure the potencial difference between the resistors.

In order to ensure the currents flowing through each resistors are the same, a cryogenic current comparator (CCC) is used [35]. The CCC is a superconducting device based on the Meissner effect, in which magnetic fields are expelled from superconductors. Consider a superconducting tube with two wires inside (Figure 3.3b); upon passing current through the wires, there is a resultant magnetic field that induces screening currents on the inner surface. The screening currents flow to the outer surface of the tube, giving rise to a magnetic field outside of the tube, which can be detected by a magnetometer. As magnetic detector the superconducting quantum interference device (SQUID) -the most sensitive magnetometer- is used; its output signal is fed back to the current source (e.g. I_2) to null the magnetic field.

The resistor to be calibrated is normally adjusted to a value different from R_K; for this purpose ratio N_p/N_s of the flux transformer (where p and s stand for primary and secondary respectively) is adjusted as close as possible to the desired ratio $\mathrm{R}_K/\mathrm{R}_S$ to be measured. The SQUID output regulates the current in the secondary in a closed feedback loop, ensuring that $N_pI_p = N_sI_s$. The detector can be balanced with the help of an additional *trim* coil N_t, a variable resistance R_l and a fixed high-value resistor R_h. The ratio to be measured is then given by [34]:

[1] R_K is the von Klitzing constant, named after the discoverer of the quantum Hall effect

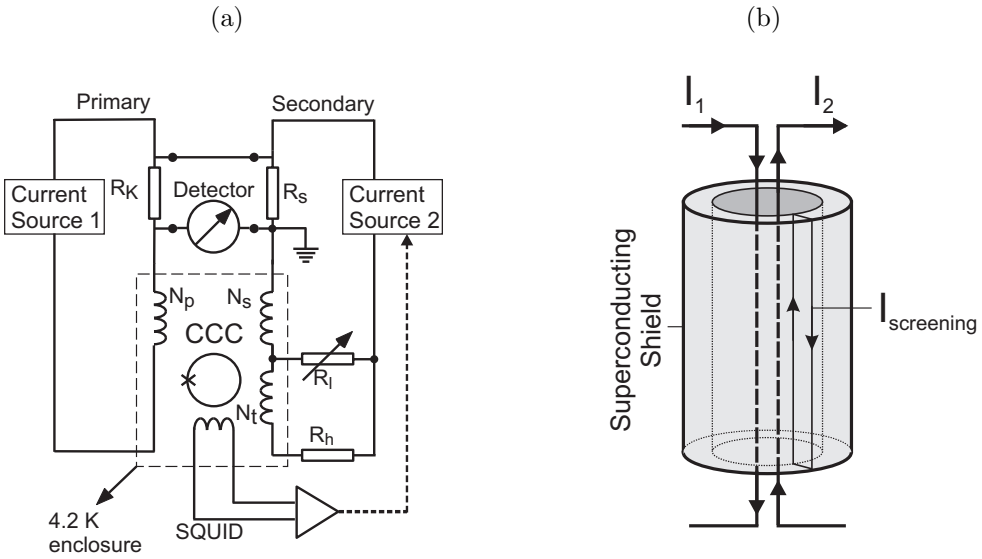

Figure 3.3: (a) Schematic of the current bridge used to compare two-resistors, R_K and R_S. The cryogenic current comparator ensures the current flowing through the two resistors is for practical purposes the same and the calibration reduces to measure the potential difference between the resistors (adapted from [34]). (b). The CCC is a superconducting device based in the Meissner effect, in which a magnetic field is expelled from superconductors by screened by screening currents at the surface. In the device shown, screening currents will flow if $I_1 \neq I_2$; the resulting surface current $I_{screening} = I_1 - I_2$ can be detected by the magnetic field it produces, using pick-up coil connected to a superconducting quantum interference device (SQUID), the most sensitive magnetometer available.

$$\frac{R_K}{R_s} = \frac{N_p}{N_s}\frac{1}{(1+d)}\frac{1}{(1+V_M/V)}; \qquad d = \frac{N_t}{N_s}\frac{R_l}{(R_l+R_h)} \tag{3.2}$$

where V_m is the detector reading ($\simeq$0) and V is the voltage drop across the resistors. Typical parameters for a comparison of the quantum Hall resistance at filling factor $\nu = 2$ ($R_K/2 \approx 12.9k\ \Omega$) against a 100 Ω standard are: $N_P = 2065$, $N_s = 16$.

Chapter 4

The quest for monolayer graphene on silicon carbide

Growth of monolayer graphene on silicon carbide (SiC) requires the controlled desorption of silicon and carbon atoms from the crystal, followed by a reconstruction at high temperatures ($T \gtrsim 1300^o$C) of the carbon atoms that remain on the surface. Unlike conventional epitaxial growth, where the temperature of the substrate (T_s) and the deposition rate ($\dot{r}$) are independently controlled to produce high quality films, sublimation of silicon from SiC involves the control of only one parameter, T_s.

An extra degree of freedom during growth can be introduced by controlling the vapour species desorbed from SiC (e.g. Si, Si_2C or SiC_2). In order to achieve this, the group of Rositza Yakimova employs an unreactive gas (1 atm of argon) to grow monolayer graphene on the silicon face of SiC. This high pressure process allows controlling the desorption of atoms from SiC and also the use of higher temperatures ($T = 2000^o$C), which lead to better crystallization and reduction of defect formation.

This chapter presents an overview of the conditions that lead to the fabrication of single layer graphene on SiC and its "observation" by means of magneto-transport measurements, which are also used to asses the quality of the as-grown monolayer in terms of carrier type, concentration and mobility.

4.1 Making electronic-grade graphene

Epitaxial graphene grown on silicon carbide is particularly attractive because of its scalability. There exist, however, alternative technologies to produce graphene suitable for electronic applications, the most popular of them are described below:

Exfoliation from graphite. The repeated cleavage of graphite to obtain a single graphene monolayer continues to be the preferred method when high quality crystalline samples with large carriers mobilities are sought. In general, graphene flakes are the closest to ideal graphene, specially when suspended, and for this reason they are often used as a test-bed for physics and proof-of-concept devices. Even though improvements to this technique have allowed the extraction of flakes as large as ≈ 1 mm^2, (which are commercially available), low throughputs limit its use to scientific research.

Chemical vapor deposition (CVD). coraux new journal of f physics 2009) An economical way to produce large area graphene is by decomposing and graphitizing an organic material on a hot surface. Metals are used as catalyst in order to decrease the temperature of the reaction; reports in literature include ruthenium, iridium, nickel, copper [36–40]. In theory this process might be self-limiting, such that growth stops when the surface of the metal is completely covered by a monolayer of carbon. In reality, defects on the metal surface cause the graphene monolayer to be polycrystalline, with grain size related to crystal domains of the metal used as catalyst. Additionally, after-growth transfer of CVD graphene onto insulating substrates typically results in heavy doping and defect formation (ripples). This type of graphene is envisioned as replacement of indium tin oxide in optoelectronics.

Epitaxial growth on silicon carbide. Silicon carbide can be used as precursor of monolayer graphene by annealing it to high temperature ($T \gtrsim 1300\ ^oC$). After silicon carbide sublimes, the carbon-rich surface can re-crystallize; precise control of growth conditions as well as careful selection of crystal type, face and orientation are required for growing a single layer of graphene. Compared to

CVD, the electronic properties of the as-grown large area monolayer graphene produced by this method are often superior in terms of carrier mobility and doping. The areas of application for this type of graphene include high frequency analogue electronics and quantum metrology. In this chapter, further details of this method are described.

4.2 The precursor: crystal structure of SiC

Over 250 different polytypes[1] of SiC have been identified up to date [41]; in all the different SiC polytypes the fundamental repeating unit is a tetrahedron formed by three silicon atoms sp^3-bonded to a carbon atom. This tetrahedron is repeated along two dimensions, and the difference between polytypes lies in the third dimension, either in the number of basal planes (Si-C bilayers) or its stacking sequence. The most abundant polytypes are the hexagonal (6H-SiC and 4H-SiC, commonly termed α-SiC) and cubic (3C-SiC, commonly referred as β-SiC). The nomenclature for the polytypes is derived from its crystal structure: H (C) refers to hexagonal (cubic) crystal structure, while the number represents the amount of stacked basal planes in a unit cell (Figure 4.1a).

An additional detail is the fact that the two "sides" of the crystal, the *faces* of the polytype, are terminated in a different way. In figure (4.1a) the carbon $(000\bar{1})$ and silicon (0001) faces for the 4H polytype have been indicated. The practical implication is that the kinetics of silicon desorption is different for the carbon and silicon faces. This leads to a faster growth of graphene on the C-face compared to the Si- face; as a consequence, annealing SiC in vacuum results on many graphene layers on the carbon face.

4.3 Multilayer graphene on the C-face

Graphene layers grown on the carbon face are rotated with respect to each other as they grow, which to some extent decouples them electronically, as if they were

[1] Compound materials may exist in different structures called polymorphs. If the polymorphs are crystalline then they are called polytypes. SiC is unique in displaying such a large amount of polytypes

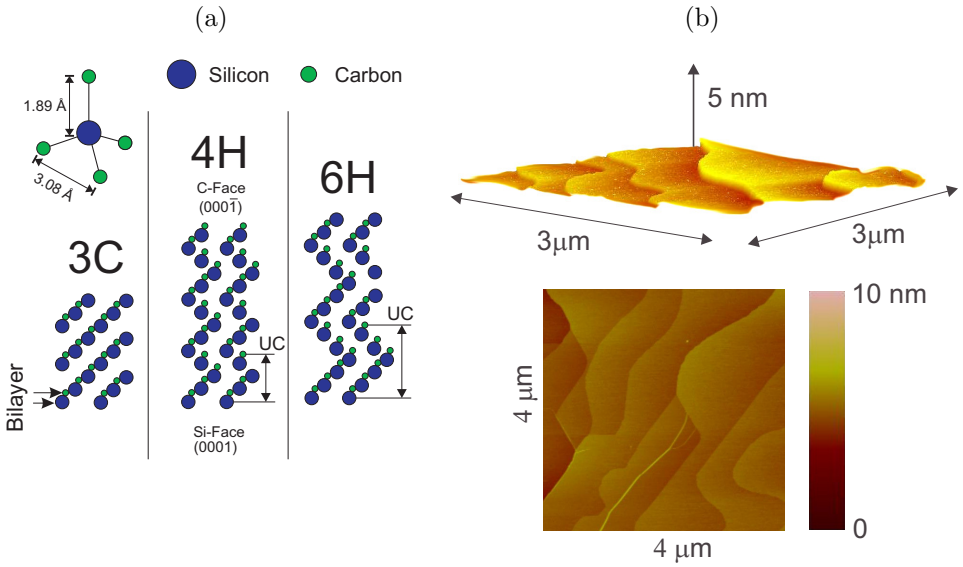

Figure 4.1: (a) The unit cell (UC) of the most common polytypes of SiC, 3C, 4H and 6H are formed by stacking 3, 4 and 6 silicon-carbide bilayers, respectively. The carbon (000$\bar{1}$) and silicon (0001) faces are indicated for the 4H polytype. (b) Atomic force microscope image of the terraces on the 4H-SiC surface after growth of monolayer graphene.

a stack of free-standing graphene layers. For this reason, this material receives the name of Multi-layer Epitaxial Graphene (MEG) and not graphite [42, 43]. MEG stacks have been found to be extremely flat and in fact its topmost layer is typically continuous over the entire surface of the SiC crystal.

Motivated by the formation of smoother surfaces over large areas, early attempts to measure electronic transport in graphene on SiC focused on the carbon face. MEG on the carbon face displayed some sort of two-dimensionality from magnetotransport measurements as a consequence of the rotational disorder. Observed phenomena included Shubnikov-de Hass oscillation [10] and weak antilocalization [44], although no half-integer quantum Hall effect was observed. The absence of this was attributed to the different degree of doping for different layers in the MEG stack, which resulted in magnetic field-dependent scattering into the N=0 Landau level of the undoped overlayers, always coincident with the Fermi energy in the transport layer [45].

To summarize, despite the undoubtfully high quality MEG stacks grown on

the carbon face, the absence of half-integral quantum Hall effect (the fingerprint of monolayer graphene in magnetotransport) raised questions about the possibility of growing a true graphene monolayer on SiC.

4.4 Single-layer graphene on the Si-face (SiC/G)

When annealed in vacuum, the silicon face of SiC becomes particularly rough and produces discontinuous graphene domains with random thickness throughout the surface. Nevertheless, the slower growth on this face suggested that a better control would be possible, and as a consequence, obtaining a single monolayer could be feasible.

With this in mind, Virojanadara et al. [11] replaced vacuum by a background pressure of inert gas (1 atm or argon) when annealing 4H-SiC. Control of pressure is the extra"knob" used together with substrate temperature to control the growth rate and quality of the graphene monolayer. This technique has been compared to what is used in incandescent light bulbs, in which an inert gas is added to prevent the evaporation of the tungsten filament increasing in this way the lifetime of the bulb [46]. The inert molecules decrease the sublimation rate of silicon carbide and also allow an increase in substrate temperature by several hundred degrees. An advantage of working at higher temperatures is that the ratio between silicon and carbon of the species in the gas phase decreases with increasing temperature, and thus a higher quality and careful control of monolayer graphene may be obtained. As a result, SiC processed using this technique displays large graphene domains ($\sim 50\ \mu$m), atomically continuous over steps separating large and flat terraces on the surface of SiC, as confirmed by atomic force microscopy (AFM) (Figure 4.1b) and ARPES.

Graphene-SiC interface

From stoichiometric considerations, roughly three silicon-carbon bilayers are needed to form a single graphene layer; since these conditions are hardly meet in reality, the consequence is the formation of a graphene-like layer growing at the interface between graphene and SiC. This interfacial layer is called zero layer or buffer

layer in literature (Figure 4.2a).

On the silicon face, the buffer layer is chemically bound to silicon atoms and ARPES measurement reveal that this layer has a band gap of about ~ 0.3 eV, which can increase due to absorption of atomic species, e.g. hydrogen. However, the buffer layer can even be metallic if only one basal plane of Si-C is consumed during growth, according to calculations [47, 48]. For the carbon face it has been observed that growth in vacuum leads to a buffer layer weakly coupled to SiC, while the use of high pressure during growth leads to the formation of a buffer layer strongly-bound to SiC similar to that on the silicon face [49].

4.5 Magnetotransport in SiC/G

In addition to surface characterization techniques, the presence of monolayer graphene on the silicon face of SiC obtained using the high temperature/pressure technique was confirmed by magnetotransport measurements through the observation of half-integer quantum Hall effect [12]. For these measurements, Hall bars were patterned on graphene grown on 4H-SiC according to section (3.1), with sizes ranging from 1 to 30 μm in width and up to 180μm in length, and using different orientations (across or along terraces on SiC). As-fabricated samples showed electron doping levels around $n = 1 - 6 \times 10^{12}$ cm^{-2}, and in some cases $n = 1 - 6 \times 10^{12}$; this initial doping was observed to increase over time ($\sim$ weeks) presumably due to adsorbates from the environment. When characterized through half-integer quantum Hall effect, samples with higher doping levels require the use of higher magnetic fields (Figure 4.3a); since the highest magnetic field available was B = 14 T, the observation of quantum Hall effect was limited to samples with carrier density $\lesssim 8{\times}10^{11}$ cm^{-2}.

The observation of plateaus in ρ_{xy} at filling factors ν=2 and ν=6, so far not observed on any epitaxial graphene on SiC, confirmed that electron transport was dominated by single layer graphene even in the longest sample (Figure 4.3b). The observation of quantum phenomena confirmed the high quality of the monolayer (electron mobility $\mu \approx 3000$ cm^{2}V^{-1}s^{-1} at room temperature and $\mu \approx 6000$ cm^{2}V^{-1}s^{-1} at T= 4 K) over large area; combined with the fact that the Hall bars go across several terraces, our findings suggested that the graphene monolayer is

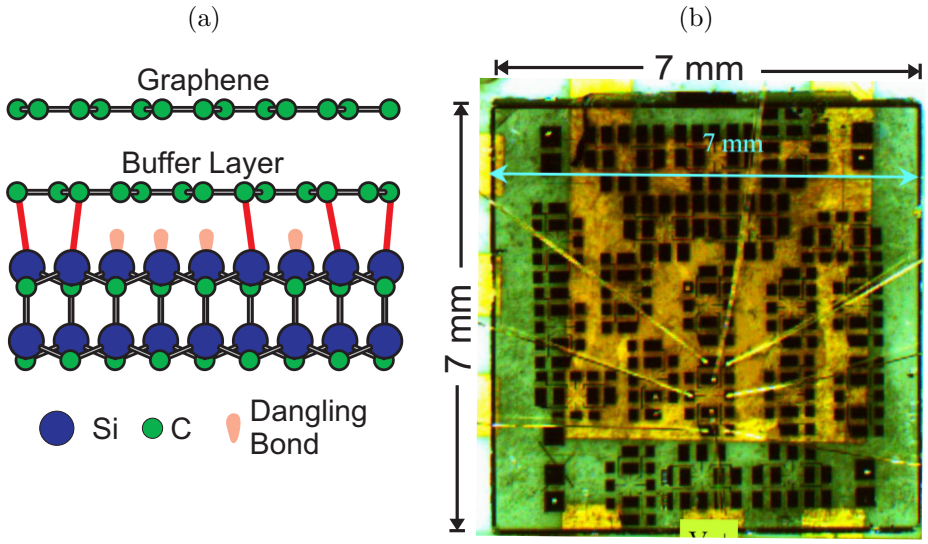

Figure 4.2: (a) Non-stoichiometric growth on the silicon face results in a *buffer* layer, a graphene-like layer covalently bonded to SiC (adapted from [50]).(b) Large area chip (7×7 mm^2) employed for experiments; on this, many Hall bars are patterned along/across the terraces on SiC. Dark squares are metallic contacts.

similar to a carpet going smoothly over the SiC steps.

Charge transfer from SiC to graphene

As-grown graphene is normally doped due to electrostatic interaction with the SiC substrate via the buffer layer. In magnetotransport, the importance in producing low-doped graphene lies in the fact that lower carrier concentrations reduce the magnetic field at which quantum phenomena, needed to identify single-layer graphene, can be observed.

The doping levels appear to be typically higher in monolayer graphene (on the silicon face) compared to MEG stacks on the carbon face. There are two reasons for this: 1) the charge-density decay length is about one monolayer so charge transfer to top layers in MEG is screened [51, 52] and 2) electronic decoupling of the layers due to rotational stacking of graphene layers in MEG minimizes the influence of the SiC substrate.

Without taking adsorbates on graphene into consideration, the doping of the

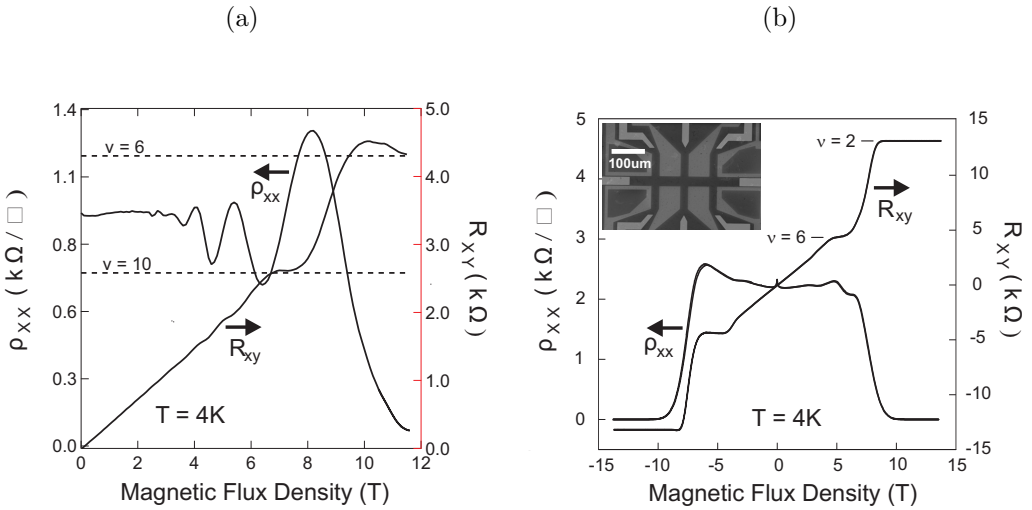

Figure 4.3: (a) Shubnikov-de Haas oscillations in a sample with electron concentration $\sim 2 \times 10^{12}$ cm^{-2}; this doping level requires a magnetic filed greater than $B = 30$ T to observe the $\nu = 2$ plateau. (b) Half-integer quantum Hall effect observed in large-area (Inset, scale bar 100 μm) SiC/G samples is used as evidence that monolayer graphene dominates electron transport.

as-grown graphene n arise from donors present in the buffer layer and in bulk of silicon carbide, with density of states γ and ρl respectively. The charge transfer from the buffer layer into graphene is governed by the work function difference between the donors and neutral graphene A, the Fermi level of doped graphene $\epsilon_F(n)$ and the geometric capacitance of the graphene layer to the substrate (Figure 4.4a). The charge balance equation for graphene referred to the Dirac point reads (REF Kopylov):

$$n = \underbrace{\gamma \left[A - \epsilon_F(n) - 4\pi e^2 dn \right]}_{\text{Buffer}} + \underbrace{\rho l}_{\text{Bulk}} \tag{4.1}$$

where l the depletion layer in SiC. Typical values are $A = 0.40$ eV, $d = 0.3$ nm and $\gamma = 5 \times 10^{12}$ eV^{-1}cm^{-2}. There is empirical evidence that the growth conditions impact on the initial doping of the graphene layer. Higher temperature and pressure result in lower carrier concentrations levels in the graphene monolayer. This can be explained to be a consequence of a better crystallization and enhanced diffusion of surface dopants deep into the bulk of silicon carbide

(minimizing γ and ρ), known to occur at temperatures $\gtrsim$ 1700 ^{o}C [53]. Hence, higher temperatures and pressure during growth lead not only to higher quality but also to more neutral monolayer graphene.

B-dependent electron transfer to graphene

An interesting finding for monolayer graphene grown on the silicon face is that the amount of charge transferred from the substrate depends on the externally applied (perpendicular) magnetic field. At high magnetic fields, when Landau levels (LL) form, there are intervals of several Tesla where the carrier density in graphene increases linearly with the magnetic field, until a saturation value n_∞ is reached.

B-dependent charge transfer to SiC/G is supported by the observed pinning of the ν=2 quantum Hall plateau combined with the anomalous behaviour of the critical current versus magnetic field. From the carrier concentration measured at low magnetic fields (n_0= 1/eR_H) it is possible to estimate the values of magnetic field values B_ν at which a quantum Hall plateaus corresponding to exact filling factor ν should develop, as $B_\nu = R_K/(\nu R_H) = en_0R_K/\nu$. Experimentally it is observed that once $B_{\nu=2}$ is reached, the quantum Hall plateau extends well beyond the maximum magnetic field available in the set-up ($B = 14$ T), as if $B_{\nu=2} \propto n_0$ was *dynamically* increasing. Furthermore, the break-down current i_c, that is, the maximum non-dissipative current that can flow through the graphene Hall bar, keeps on increasing well beyond $B_{\nu=2}$. This has to be contrasted with conventional two-dimensional systems, where the critical current reaches a maximum when the magnetic field fulfils the exact filling factor condition B_ν (see figure 4.4b) and then decreases. The excess charge can be explained using figure 4.4b, in which at filling factor $\nu = 2$ the Fermi energy coincides with the partially filled $N = 0$ LL ($\epsilon_F = 0$). In this situation, the saturation carrier density can be calculated using equation 4.1, from which $n_\infty = A\gamma/(1 + 4\pi e^2\gamma d)$. Hence, at high magnetic fields, when the density of states discretizes into Landau levels, the buffer layer and substrate act as a reservoir that keeps on *filling* the Landau levels beyond the initial carrier density n_0. The final carrier concentration of graphene is determined mostly by the density of donor states γ (d is small, $\approx 3 - 4$ Å), which can be to

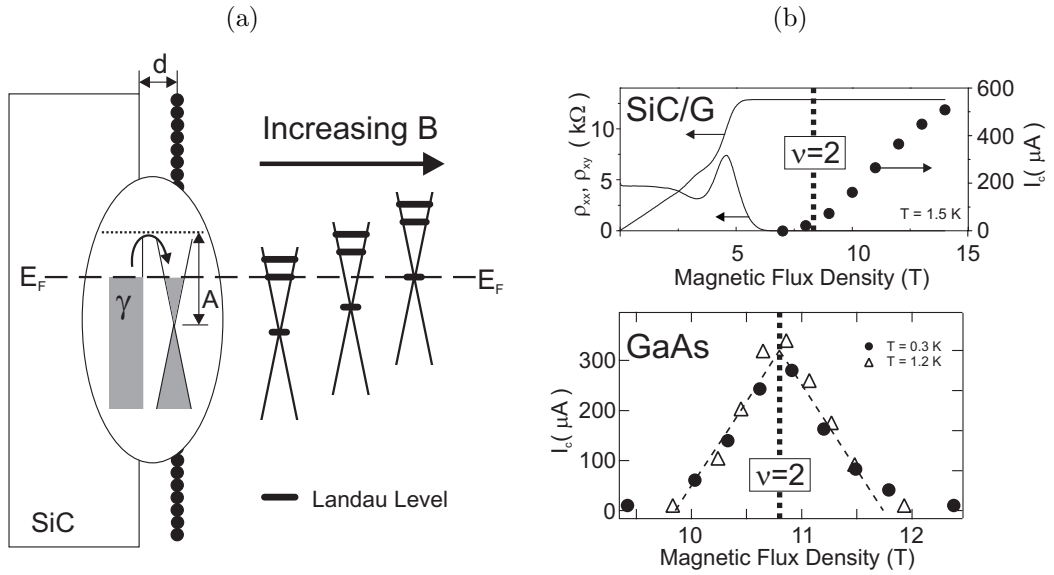

Figure 4.4: (a) Electrostatic interaction of graphene with the SiC substrate via the buffer layer leads to a magnetic field-dependent electron transfer to graphene; it has been experimentally observed that the N=0 Landau level remains completely filled over an exceptionally broad range of magnetic field [54]. (b) The pinning of the N=0 Landau level manifests as an enhanced critical current in epitaxial graphene on SiC; compared to GaAs heterostructures (adapted from [34]) in which i_c reaches a maximum at exact filling factor (center of a plateau), for epitaxial graphene the critical current keeps on increasing and reaches $I = 0.5$ mA.

some extent controlled (lowered) by high temperature/pressure growth [11].

Thus, uniquely to monolayer graphene on the silicon face, the strong interaction with the substrate via the buffer layer is such that Landau levels (in particular, the one at exactly zero energy) remain completely filled over an exceptionally broad range of magnetic fields. Large and flat quantum Hall plateaus combined with the high non-dissipative current in the quantum Hall regime have important implications for application of SiC/G in quantum metrology (Chapter 7).

4.6 Summary

High temperature (T = 2000 ^{o}C) and pressure (1 atm of Argon) have been established as suitable conditions for the growth of a single layer of graphene on the

silicon face of 4H-SiC. This material is particularly suitable for electronic applications (large-area) and as such, magnetotransport is the ultimate tool to asses the quality of the material in terms of carrier type, concentration and mobility, as well as layer count when employing high magnetic fields. As-grown material is typically doped at levels $n_0 \approx 1 - 10 \times 10^{12}$ cm^{-2} and this can increase at high magnetic fields ($B_{\nu=2}$) to a saturation value n_∞. The initial and final carrier concentration are a consequence of the interaction with the substrate and donors in the buffer layer, produced during growth; higher temperature/pressure seem to result in lower n_0 and n_∞.

Chapter 5

Carrier density control in SiC/G

A complete electrical characterization of SiC/G requires the possibility to control its carrier density; lower carrier concentrations allow the study of quantum effects at lower magnetic fields. For example, with a magnetic field of B = 10 T, the maximum carrier concentration at which the $\nu = 6$ and $\nu = 2$ quantum Hall plateaus (needed to distinguish monolayer from bilayer graphene) can be observed is $\lesssim 4 - 8 \times 10^{11}$ cm^{-2}.

The growth conditions described in Chapter 4 reliably produce electron-doped SiC/G with initial density of n ∼5-10×10^{11} cm^{-2}, but when the sample is left unprotected (i.e. exposed to air) or after microfabrication, the carrier concentration can increase to levels $\sim 1 \times 10^{13}$ cm^{-2} resulting in unfeasibly high magnetic fields needed to observe half-integer quantum Hall effect.

The thick, insulating SiC substrate makes it difficult to emulate bottom gating schemes employed in exfoliated flakes to electrostatically control its carrier concentration. A top gating is therefore the natural choice in SiC/G, but the gate dielectric has to be carefully chosen, since direct contact with the graphene layer can degrade its electronic properties.

This chapter describes the techniques developed to control and preserve the carrier concentration of SiC/G, based on organic polymers; these include electrostatic top-gates, non-volatile photo-gating and a solid electrolyte.

5.1 Encapsulation with organic polymers

Soon after the discovery of graphene its sensitivity to adsorbates was noticed and exploited to develop sensors that displayed changes in electrical conductace in reponse to the presence of single molecules [55]. Graphene is thus prone to unintentional doping and if its carrier concentration is to be controlled, the samples must be protected from adsorbates present in the ambient (Figure 5.1a).

Graphene can be protected from the ambient by encapsulating it with a material that preserves its electronic properties (carrier concentration and mobility) while at the same time providing a barrier against adsorbates. Inorganic materials (i.e. oxides), typically deposited by evaporation or sputtering, are known to introduce electron scatterers in graphene due to poor stoichoimetry during evaporation. The exception might be those oxides deposited using Atomic Layer Deposition (ALD), not readily available in every microfabricaiton facility.

A simple and inexpensive solution to encapsulate graphene is by coating it with organic polymers (Figure 5.1b) [56]. In particular, we found that poly(methyl methacrylate- co -methacrylate acid) (PMMA/MMA) introduces a minimum amount of additional electron doping ($\lesssim 1 \times 10^{11}$ cm^{-2}) with virtually no carrier mobility degradation. Additionally, it displays good resistance to water and thermal cycling, necessary for electrical measurements at low temperatures. This polymer is normally used as a lift off layer for e-beam lithography and is available from several suppliers. More details are provided in Appendix A.

Another way to protect graphene is using Teflon® Amorphous Fluoropolymer, which can be spun onto graphene and form thin films (t<1 μm) in the same way as PMMA/MMA. This fluoropolymer provides most of the advantages associated with teflon, specially the resistance to many chemicals with the exception of fluorinated solvents. The main disadvantage is associated with the hydrophobicity of Teflon, which complicates further microfabrication due to poor adhesion of organic resists. Nevertheless, this problem can be circumvented if necesary by, for example, evaporating a metal (Al or Ge) on top of Teflon® AF to enable spin-coating with resists needed for further lithography steps.

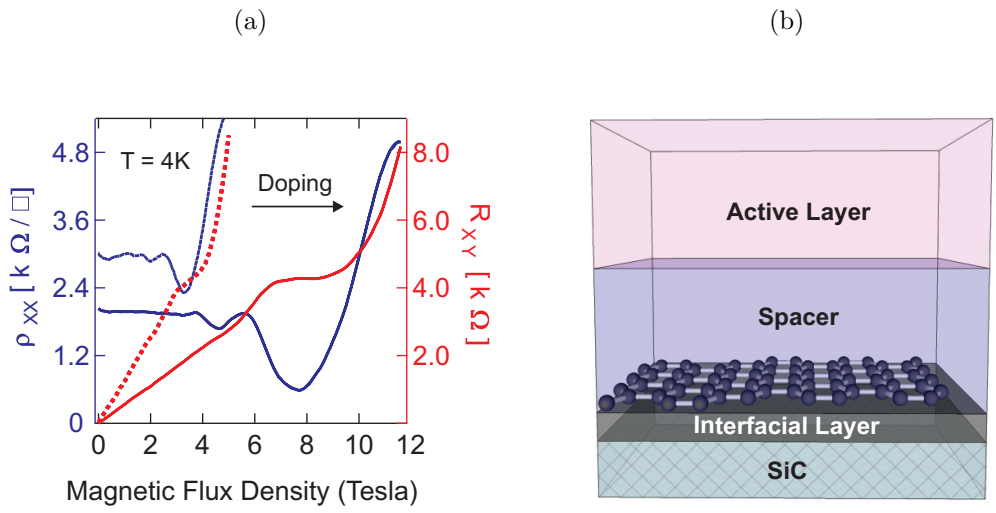

Figure 5.1: (a) Extra doping in the bare sample after thermal cycling, between $T = 4$ K and room temperature, increases the magnitude of magnetic fields where half-integer quantum Hall effect can be observed. (b) SiC/G can be protected by encapsulating it with organic polymers; the spacer protects the electronic integrity of the monolayer by decoupling it from the active layer, which can be a metallic gate or another polymer.

5.2 Electrostatic carrier control

When exfoliated graphene flakes are deposited on Si/SiO_2, the heavily doped silicon is used as a (bottom) electrostatic gate separated from graphene by a thin silicon dioxide layer (.3 μm). In SiC/G, a similar scheme is not possible due to the thickness of SiC (300 μm). Bottom gating of SiC/G has been demonstrated nonetheless by ion implantation on the surface of SiC prior graphene growth[57]; besides resulting in low-mobility graphene, this process is not easily implementable.

The natural alternative is a top gate electrode. Except for atomic layer deposition (ALD) of Al_2O_3 [58] or HfO_2 [59], (non-stoichiometric) deposition of inorganic compounds degrades the electronic properties since dangling bonds can react with graphene and form carbides, destroying the monolayer, or act as electron scatterers, reducing substantially the electron mobility.

Having proved harmless to SiC/G, the organic polymers PMMA/MMA and Teflon® AF were employed as dielectric for metallic top gate electrodes, which were evaporated through a shadow mask. A quick estimation for the performance of a gate dielectric is the maximum surface charge that can be induced in the dielectric Q_{Max}=$\varepsilon_r\varepsilon_0 E_{Max}$, given its dielectric strength E_{Max} and permitivity $\varepsilon_r\varepsilon_0$. For both materials, $\varepsilon_r \approx 2-3$ and dielectric strength can in principle be up to an order of magnitude higher for thin films of Teflon® AF [60–62], such that $Q_{Max,Teflon} \approx 6 \times 10^{12}$ cm^{-2}.

In practice PMMA/MMA performed better; a 300 nm-thin layer could sustain up to $V_G = 60$ V before breakdown while the fluorinated polymer leaked at $V_G = 10$ V; this was attributed to the presence of pinholes. Thinner PMMA/MMA films resulted in less robust dielectrics, due to inhomogeneous coverage of graphene. The maximum tuning of carrier concentrtion using electrostatic gate was in the order of $\Delta n \sim 1 \times 10^{11}$ cm^{-2} and the effective dielectric strength and capacitance for PMMA/MMA was $E_{Max,PMMA} \approx 200$ MVm^{-1} and C$\approx$ 100 pFcm^{-2} (Figure 5.2b).

5.3 Photochemical gating

There exists applications where carrier control is needed but the inclusion of a gate electrode can be detrimental due to additional electrical noise. For this purpose we developed a reversible, non-invasive and non-volatile way to control the carrier concentration in SiC/G usign light as a "gate". This method is based on the photosensitive, chlorinated poly(methyl styrene- co -chloromethyl acrylate), comercially available as ZEP520.

The photo-gateable heterestrocture is formed by coating the sample with PMMA/MMA, as described in the previous section, followed by ZEP520 deposited from solution by spin-coating (for details see Appendix A) (Figure 5.2a). The carrier concentration of as-grown SiC can be decreased by $\Delta n \sim 2-3 \times 10^{12}$ cm^{-2} when exposing this heterostructure to deep ultra violet light (DUV), with wavelength $\lambda = 248$ nm. The carrier concentration can be restored back to its original value by heating the heterostructure above the glass transition temperature ($T_g \approx 170$ ^{o}C).

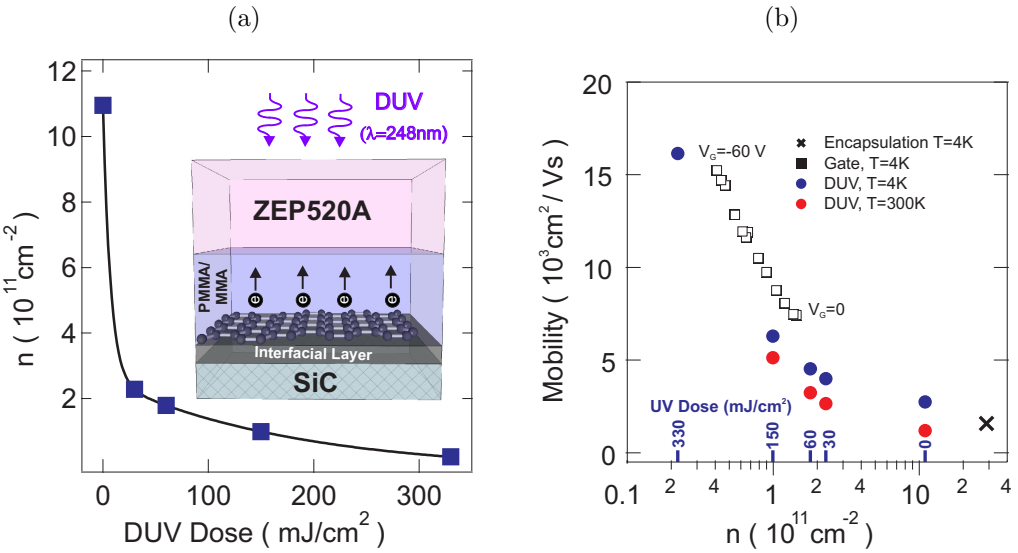

Figure 5.2: (a) Carrier density control with deep UV light ($\lambda = 248$ nm) using a polymer-SiC/G heterostructure.(b) Comparison of mobility and range of carrier density control for photochemical and electrostatic gating.

The mechanism of photochemical gating is explained due to formation of electron acceptors in ZEP520A upon irradiation with DUV (or equivalently with e-beam), causing electrons in SiC/G to diffuse through PMMA/MMA and be trapped in ZEP520A. It was observed that a second layer of ZEP520 decreased further the electron concentration in graphene confirming the bulk nature of the photochemical gating. Also, in a control experiment, exposing SiC/G coated ony with PMMA/MMA produced the opposite effect of increasing the electron concentration by $\Delta n \sim 1 \times 10^{12}$ cm^{-2}. The gating process can be optimized by modifying the thickness of the spacer polymer. A thinner PMMA/MMA (50 nm) leads to a stronger effect of illumination, although for thinner PMMA/MMA layers or with ZEP520A deposited straight on graphene we observed a reduction in mobility.

The electron traps in ZEP520 are thought to be highly electronegative chlorine atoms that separate from the polymer backbone upon high-energy irradiation (Figure 5.3a). The formation of radicals in irradiated ZEP520 was confirmed

with Electron Paramagnetic Resonance (EPR)[1]. For such analysis the solvent of ZEP520 (anisole) was evaporated in a convection oven and the EPR spectrum was recorded before and after irradiation with a mercury vapor lamp; it was found that radicals are absent prior irradiation or after annealing to $T = 170\ ^{o}$C (Figure 5.3b). Further studies to confirm chlorine as the source of unpaired spins will be pursued in the future.

The practical implications of the photochemical gating are the enhancement of carrier mobilities up to 16,000 $cm^2V^{-1}s^{-1}$ at T = 4 K and 5,130 $cm^2V^{-1}s^{-1}$ at room temperature (Figure 5.2b. The irradiated devices have shown to preserve the carrier concentration over long periods ($\sim$ years) and have been of great importance in quantum metrology for the development of a new electrical resistance standard (Chapter 7).

5.4 Solid electrolyte

The natural process variabilty of the high temperature/pressure growth of SiC/G ocasionally results in high doping levels, n$\sim 1 \times 10^{13}$ cm^{-2}. In this case neither electrostating gating using organic polymers as dielectric nor photochemical gating are sufficient to decrease the carier concentration low enough to allow for complete electrical characterization.

There are reports in literature where solid electrolytes are employed to control the carrier concentration of graphene at levels in excess of n$\sim 1 \times 10^{13}$. These materials are widely used in battery technology and consist of an ionic compound dissolved in a polymer matrix through which the ionic species can diffuse upon applying a voltage. When gating graphene, polyethylene oxide (PEO) has been used as a polymer matrix and lithium perchlorate ($LiClO_4$) as the ionic salt, but a problem associated with this system is that graphene can be irreversibly oxidized/reduced by the free ions ClO_4^-/Li^+ [63].

[1]EPR is technique based in energy transitions between Zeeman-splitted energy levels of unpaired electron spins. A sample containing radicals is irradiated with frequency f and absorption is recorded as the magnetic field B is varied; absortion will occur whenever $hf = g_e \mu B_0$, where h is the Planck constant, g_e is the Landè g-factor and μ_B is the Bohr magneton. Interpretation from spectra is non-trivial, but the number of absorption peaks can provide information about the electronic structure of the radicals

(a) (b)

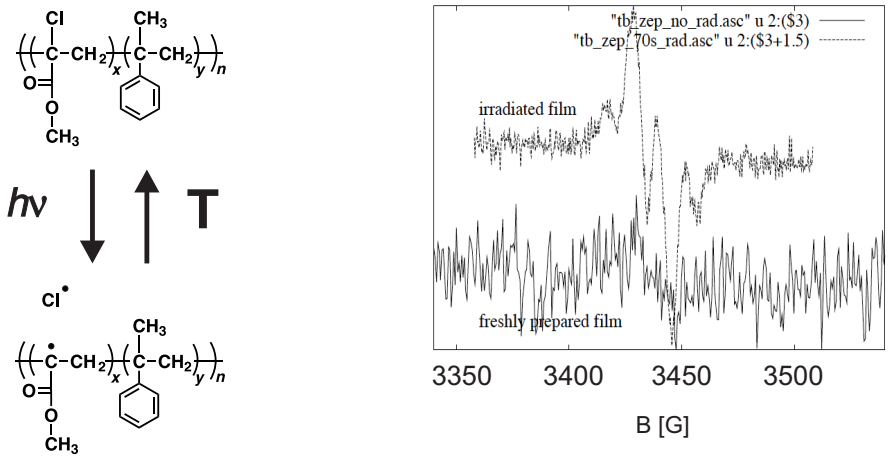

Figure 5.3: (a) Bond breaking of chlorine atom from the polymer backbones is proposed as the mechanism responsible for the observed photo-gating. (b) EPR spectrum of ZEP520 before and after irradiation confirms the presence of unpaired electrons after irradiation with deep UV.

We have replaced lithium perchlorate with lithium triflate (CF_3SO_3Li) as ionic compound and this has resulted in a robust and reliable way to tune the carrier concentration of graphene at the level $\Delta n \sim 2 \times 10^{13}$. As-grown SiC/G is tipically electron doped, which implies that carrier reduction can be achieved by placing negative ions in close proximity to graphene. In the case of $CF_3SO_3^-$, the electron is delocalized over the entire ion, which suppresses substantially its chemical reactivity compared to $LiClO_4$. For preparation details see Appendix A.

Typical $\rho_{xx}(V_G)$ and $\rho_{xy}(V_G)$ are shown in figure 5.4a, where it is observed a crossing of the Dirac point at $V_G = -1.4$ V. In this gating scheme, upon applying a gate voltage, ions diffuse through PEO until the surface of graphene is decorated by ions sitting at a distance equal to the Debye length ~ 4 Å from graphene; the graphene/double layer/ions as a parallel plate capacitor results in a large capacitance that enables the use of coplanar gate electrodes. The gates are fabricated also with graphene in order to prevent electrochemical reactions with metals; in a structure with a gate-channel gap of 20 μm, voltages up to V_G=10

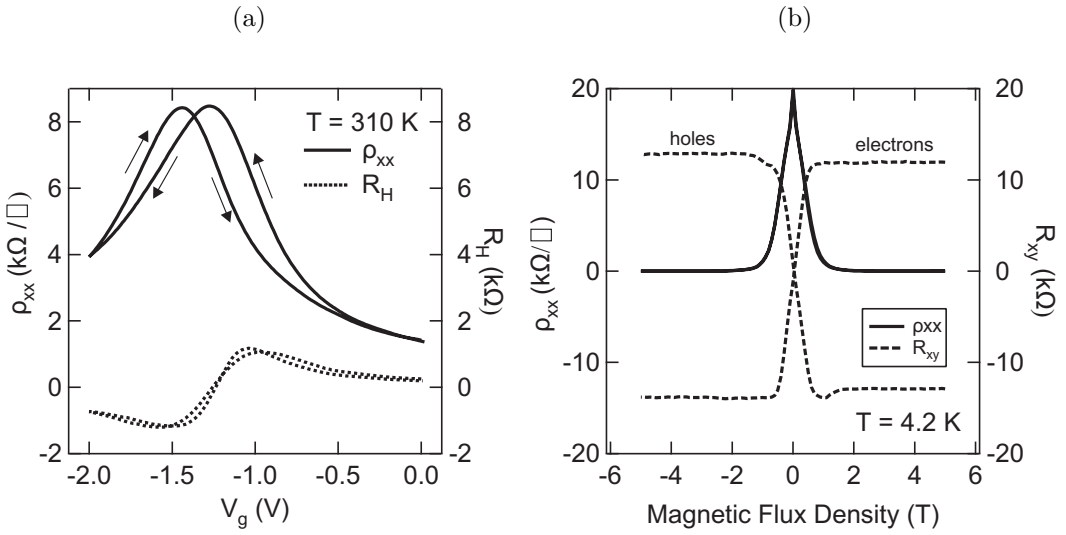

Figure 5.4: (a) Gate trace using lithium triflate as solid electrolyte at room temperature and coplanar graphene gate. Crossing of the Dirac point occurs at $V_G = -1.4$ V; the hysteresis in the traces is decreased at higher temperatures (the maximum used was $T_{Max} = 320$ K) or slower gate sweep rates ($\dot{V}_G = 200$ mV/min). (b) Magnetotrasport at 4K displaying onset of $\nu = 2$ plateau for electron and hole concentration (positive and negative slope of ρ_{xy} respectively) at magnetic fields $B \sim 1$ T.

V have been applied without any degradation of SiC/G.

Limited by the diffusion of ions, this gating scheme works only at temperatures above T = 220 K and better results (faster response to the applied V_G and less hysteresis in $\rho_{xx}(V_G)$) are obtained above room temperature, with T = 380 K the maximum tested temperature. In order to set the carrier concentration (n) of SiC/G to a desired value, the gate voltage is applied at room temperature and n(V_G) is measured through R_H at low magnetic fields (B< 1 T). Once the desired V_G is identified, all the contacts in the Hall bar are grounded and V_G is applied prior cooling; this results in more homogeneous doping profile in the sample as revealed by a flat $\rho_{xx}(B)$ at T = 4 K. At low temperatures, T < 220 K, the gate voltage can be removed and the carrier concentration will remain frozen.

5.5 Summary

The carrier concentration in as-grown SiC/G can be preserved by encapsulation with the polymers PMMA/MMA or Teflon® AF. As carrier control methods we employ a metallic top gate deposited onto organic dielectrics, photochemical gating or solid electrolytes, which allow to tune the carrier concentration in SiC in the order of $\Delta n \sim 1 \times 10^{11}$, $\sim 1 \times 10^{12}$ and $\sim 1 \times 10^{13}$ respectively (Figure 5.5). Each method provides its own pros and cons, and the choice was made based on the initail doping of as-grown SiC/G and the desired application.

In particular for the photochemically gateable heterostructure, the use of a neutral spacer and an active layer on top can be used as a prototypical architecture for graphene-based sensors, where the active layer is functionalized to respond not only to light but to a specific stimulus which can be sensed by graphene, protected by the spacer.

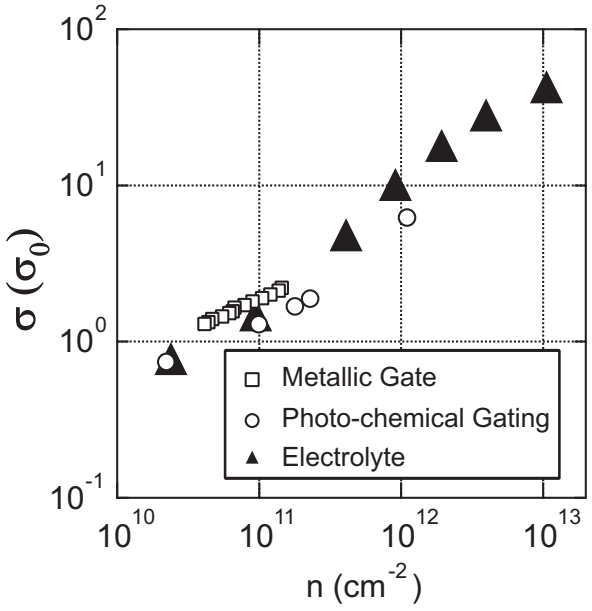

Figure 5.5: Comparison of gating techniques

Chapter 6

Quantum corrections to charge transport in SiC/G

In SiC/G the two-dimensional system is formed by the conducting graphene layer situated on top of a non-conducting buffer. The interplay between these two layers, unavailable in graphene flakes, epitaxial graphene on the C-face or semiconductor-based 2D gases, makes SiC/G a system full of rich new physics. From an application viewpoint, the development of future graphene-based devices necessitates the understanding of scattering processes that disturb the propagation of electrons in this material.

Our route to study the limits to electron mobility in SiC/G is through the analysis of quantum mechanical corrections to its conductivity. In particular, the study of weak localization provides information about inelastic and elastic scattering processes. Such analysis can shed light on the effect of, for example, adsorbates on graphene, terraces on SiC or the buffer layer. After subtraction of the weak localization (WL) correction to our measurements, we found a remaining temperature-dependent correction; this effect was ascribed to electron-electron (e-e) interactions. Compared to graphene flakes, for large-area SiC/G structures the analysis of quantum corrections to conductivity is not complicated by additional mesoscopic phenomena (i.e. mesoscopic fluctuations).

6.1 Electron scattering in SiC/G

For SiC/G, its main technological advantage is paradoxically the main mobility-degrading mechanism. The graphene layer grows on the entire surface and is well coupled to the substrate. Strong coupling of electrons in graphene with phonons in SiC result in mobilities of the order of 1,000-3,000 $cm^2V^{-1}s^{-1}$ at room temperature. Decoupling from the substrate can be achieved by hydrogen intercalation [50], suppressing in this way the effect of phonon.

In our studies, SiC/G are not decoupled from the substrate (i.e. hydrogen intercalated); for this reason we limit our analysis to low temperatures where the effect of phonons can be neglected ($T < T_{BG}$, with the Bloch-Grüneisen temperature $T_{BG} \approx 35$ K). Additionally, encapsulating SiC/G with organic polymers provides additional protection to graphene. In our encapsulated samples the maximum observed room temperature mobility is about 5,500 $cm^2V^{-1}s^{-1}$ (at n=1×10^{11} cm^{-2}) (Figure 5.2b).

6.2 Experimental steps

At low temperatures, it was observed that in addition to localization effects ($\Delta\rho_{WL}$), electron-electron interactions ($\Delta\rho_{e-e}$) also play a role in the conductivity of SiC/G. The measured resistance takes the following form:

$$\rho_{xx}(T) = \tilde{\rho}_{xx} + \Delta\rho_{WL}(T) + \Delta\rho_{e-e}(T) \tag{6.1}$$

where $\tilde{\rho}_{xx}$ is the classical Drude term. In two-dimensions both terms introduce a $\propto \ln(1/T)$ correction to $\tilde{\rho}_{xx}$, which complicates their distinction simply from the temperature dependence of $\rho_{xx}(T)$. Nevertheless, $\Delta\rho_{WL}$ can be suppressed experimentally by applying a (perpendicular) magnetic field; for this reason magnetotransport is used to distinguish the effect of weak localization from the electron-electron interaction. Experimentally, the steps followed are listed below:

1. **Estimate analytically the term $\Delta\rho_{WL}$.** This is achieved by fitting magnetotransport measurements (at a fixed temperature T_i) to the theory of weak localization in graphene. The characteristic scattering times are ex-

tracted from the fits and then, using equation 2.20, the zero-field correction is found. This "theoretical" value is denoted as $\Delta\rho_{WL,Fit}$

2. **Subtract the analytical correction $\Delta\rho_{WL,Fit}$ from measurements.** The result is a WL-corrected measurement resistance denoted as:

$$\tilde{\rho}_{xx,Theory} = \rho_{xx}(T_i) - \Delta\rho_{WL,Fit}(T_i) \tag{6.2}$$

3. **Suppress experimentally the weak localization term ($\Delta\rho_{WL} = 0$).** This is done by applying a perpendicular magnetic field. In principle, the measurement of $\rho_{xx}(T)$ under these conditions should experimentally provide the classical Drude term, here denoted as $\tilde{\rho}_{xx,Exp}$:

$$\tilde{\rho}_{xx,Exp} = \rho_{xx}(T) - \cancelto{0}{\Delta\rho_{WL}} = \rho_{xx}(T) \tag{6.3}$$

4. **Check for consistency.** By comparing the quantities (6.2) and (6.3) it is possible to know if the weak localization effects have been successfully subtracted from the measurements: when $\tilde{\rho}_{xx,Theory} = \tilde{\rho}_{xx,Exp}$ the WL term is completely subtracted from measurements.

The results from such analysis are discussed in the following sections. It was indeed found that after the WL correction is subtracted from measurements (Section 6.3), ρ_{xx} remains temperature dependent and this effect is ascribed to electron-electron interaction (Section 6.4).

6.3 Weak Localization Effects

In our samples weak localization (negative magnetoresistance) was observed at all temperature (25 mK <T< 100 K), emphasizing the role of intervalley scattering in SiC/G (Figure 6.1a). In fact, negative magnetoresistance has been systematically observed in all the samples produced so far (~ 10).

The result of the analysis is summarized in figure 6.1b, which presents all the characteristic lengths $L_{\phi,i,*}$ extracted from fitting magnetoresistance measurements of two samples, S1 and S2, to theory (eq.6.2). It was found that the

fastest process is intravalley scattering. By referring to section (2.3.2), it is then suggested that long-range potentials (e.g. charged impurity scattering) determine the electron momentum relaxation rate (the mean free path is $\ell \sim 50$ nm). Such impurities can be donors in the buffer layer.

The intervalley scattering (arising from atomically-sharp defects) is much slower. By quantifying it in terms of the mean free path ℓ it is interesting to note that the observed large values of $L_i/\ell \approx 3$ for sample 1 and $L_i/\ell \approx 6$ for sample 2 confirm that the graphene monolayer is essentially decoupled from the underlying SiC lattice. In graphene flakes, it has been observed that the edges play a role in determining the amount of intervalley scattering: narrower samples display enhanced intervalley scattering. For our large samples ($w = 30$ μm, $L = 160$ μm) edges are thought not to play a role; however, the strong intervalley scattering might be a consequence of terraces on SiC. This requires further investigation by e.g. carefully placing a Hall bar along or across the steps on SiC.

It is interesting to notice that the decoherence length L_ϕ reaches the $\sim \mu$m scale at the lowest temperature, similar as for exfoliated flakes. More details associated to this characteristic length are discussed below.

Carrier density dependence of τ_ϕ

Theory indicates that the WL correction should be independent of carrier density n when the momentum relaxation is caused by charged-impurity scattering [64]. In the polymer-encapsulated samples the carrier concentration can be changed only in a limited range. Nevertheless, we investigated $\tau_\phi^{-1}(n)$ using electrolyte gating, which allows to change carrier concentration in the range of 10^{13} cm^{-2}. Using this approach in a third sample, S3, it was found that the decoherence rate is approximately constant ($\tau_\phi^{-1} \sim 2.5$ ps) over almost three orders of magnitude in n (electrons) (Figure 6.2a). Future studies will be focused in studying decoherence when transport is due to holes.

Temperature dependence of τ_ϕ

For graphene on silicon carbide we found that L_ϕ reaches the micrometer range at the lowest temperature, the same length scale as in exfoliated graphene flakes

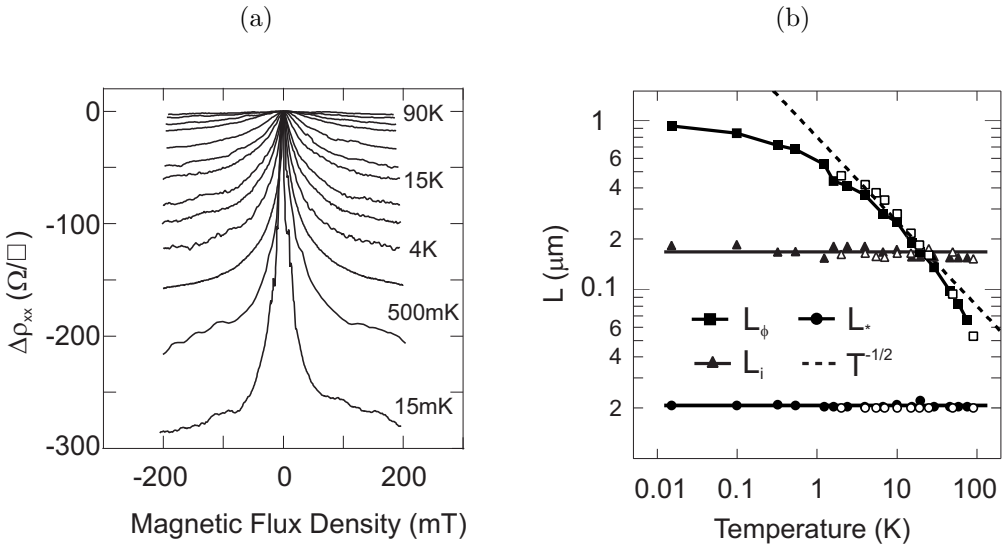

Figure 6.1: (a) Weak Localization observed at all temperatures reveals coherent transport in SIC/G and the effect of intervalley scattering. (b) Characteristic scattering lengths obtained from fit to theory (eq.2.20).

[65]. In contrast with observations on flakes [65] we did not find any indication of saturation of L_ϕ (although close to T = 0 a slower temperature dependence was observed). This finding is attributed to proper filtering of high frequency electromagnetic noise in our experimental set-up (section 3.3). Filtering excludes the effect of decoherence due to overheating of the electron system, which might be responsible for the aparent saturation of L_ϕ in previous studies.

The origin of decoherence was investigated through the temperature dependence of the decoherence rate, obtained as $\tau_\phi^{-1} = D/L_\phi^2$, with D the diffusion coefficient. Displayed in figure (6.2b), τ_ϕ^{-1} was found to saturate at a value around $\tau_s \sim 50$ ps, for the lowest temperature . We propose that the origin of this is the presence of magnetic impurities, which might be due to contamination introduced during fabrication or due to vacancies on the graphene layer, expected to be magnetic [66–68] With the idea of magnetic impurities in mind, we measured WL corrections in the presence of an in-plane magnetic field. Preliminary results show that the decoherence length increases by almost 50% when $B_{parallel} \sim 1$ T is applied (Figure 6.3a). Even though more studies are needed, this observation re-

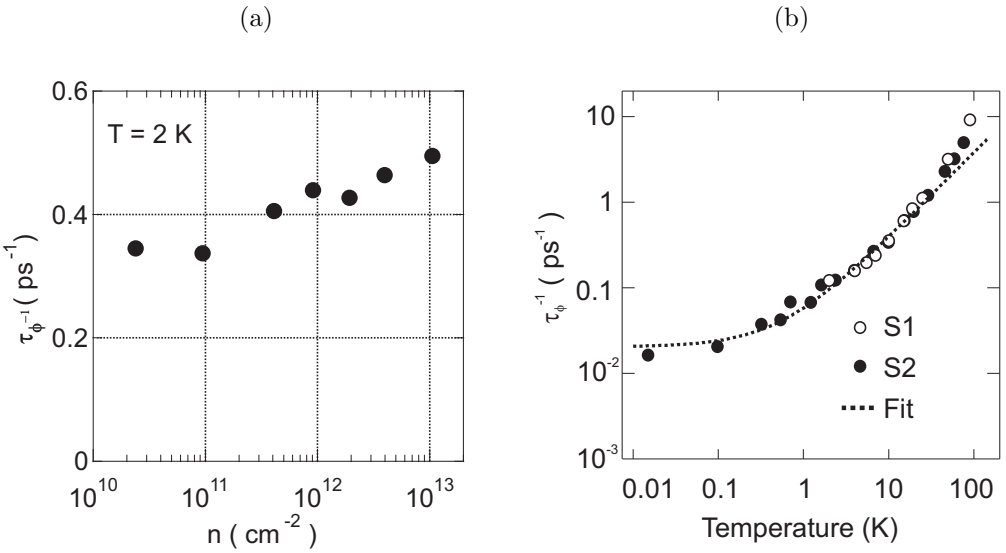

Figure 6.2: (a) Decoherence rate versus carrier concentration obtained using a solid electrolyte to change n (electrons) over almost three orders of magnitude. (b) Temperature dependence of the decoherence rate τ_ϕ^{-1} in SiC/G obtained from the WL analysis. Linear-in-T dependence signals the effect of electron interactions, while saturation at the lowest temperature is attributed to magnetic impurities, since the experimental set-up is properly filtered and heating is discarded.

veals that mechanism of dephasing "interacts" with the applied parallel magnetic field, supporting so far the hypothesis that magnetic impurities are the source of decoherence. More studies will be pursued in the future [69].

At higher temperatures, the decoherence rate displays a linear-in-temperature dependence, suggesting the electron-electron scattering as the source of decoherence. In addition, after subtraction of the WL correction from our measurements there exist a residual temperature dependence (Figure 6.3b). Given the fact that phonon contribution at this low temperature is neglected, the remaining temperature dependence is ascribed to the effect of electron-electron interactions.

6.4 Electron-electron interaction effects

After subtraction of the weak localization correction, the resistance of SiC/G displayed a residual temperature dependence, *increasing* its value as the sample

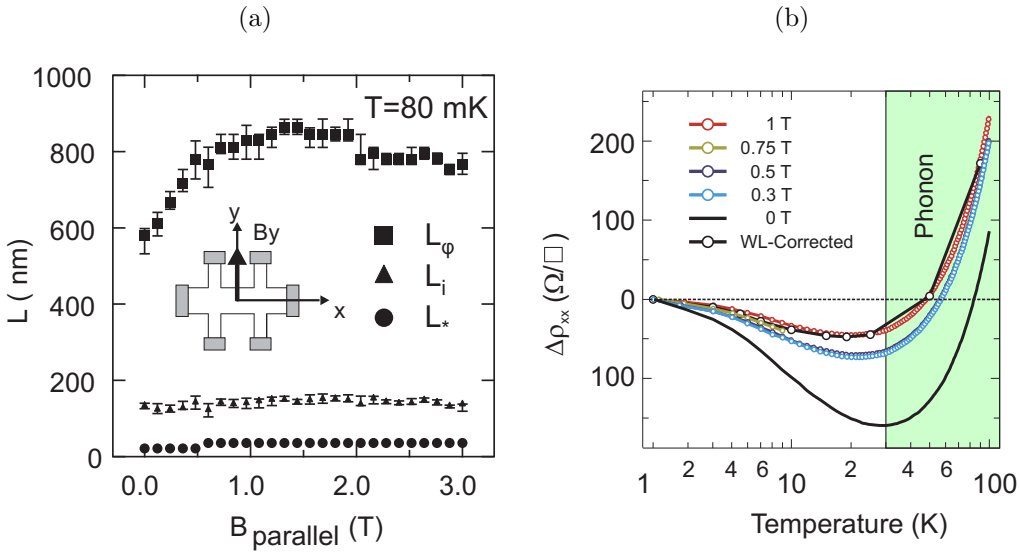

Figure 6.3: (a) Characteristic lengths obtained from the weak localization analysis in the presence of a magnetic field in the plane of graphene (B_y). The observed increase in the decoherence length L_ϕ points towards magnetic impurities being the source of dephasing in SiC/G. (b) Weak localization-corrected resistivity of SiC/G; the residual temperature dependence is attributed to electron-electron scattering. The analysis is limited to $T \lesssim 30$ K to avoid phonon contribution.

temperature *decreased* (Figure 6.3b). Together with the observed $\tau_\phi^{-1} \propto T$ (Figure 6.2b) and based on the Aronov-Altshuler theory (AA) for electron-electron interactions in the presence of disorder [64], we suggest this to be the remaining scattering mechanism.

An additional evidence supporting the effect of e-e interactions is the temperature dependence of the Hall coefficient, presented in figure 6.4. According to the AA theory, the e-e interaction corrections are present only for the Hall resistance (that is R_H), and **not** for the Hall conductivity (σ_{xy}). It was indeed observed that R_H displays a logarithmic increase as the temperature approaches zero while σ_{xy} is esentially constant in the temperature range of interest ($T < 30$ K). The observed R_H cannot be explained only in terms of an increase of carrier concentration with temperature (recalling that $R_H = 1/ne$), since any change in the carrier density would have effect on both R_H and σ_{xy}.

Continuing with the analysis of $R_H(T)$, the nature of the e-e interaction can be

understood through the ratio of (corrections to the Hall coefficient)/(corrections to the longitudinal resistance) [64]:

$$\frac{\Delta R_H}{R_H} = \frac{R_H(T) - R_H(T_0)}{R_H(T_0)} = \gamma \frac{R_{xx}(T) - R_{xx}(T_0)}{R_{xx}(T_0)} \tag{6.4}$$

The coefficient γ can take different values: a) $\gamma = 0$ in the absence of electron interactions [70], b)$\gamma = 2$ in the presence of electron interactions and c) $\gamma > 2$ for the cases of electron interactions with spin-orbit coupling. The numerical value extracted from our measurements[1] $\gamma \approx 2$ for the two samples, confirming further the effect of interactions in the system (Figure 6.5a).

At this point there are three different evidences that confirm the effect e-e interactions as the remaining scattering mechanism. These are the temperature dependence of: 1) decoherence rate (Figure 6.2b), 2) WL-corrected measurements (Figure 6.3b) and 3) Hall coefficient (Figure 6.4a). The next step is to quantify the strength of this interaction, with the intention to compare our SiC/G with other graphene systems.

Quantifying electron interaction effects

The implications for electron transport of the e-e interactions in the presence of disorder have been studied by (REF AA). In its simplest approximation, the temperature dependence of the conductivity takes the form:

$$\Delta\sigma_{e-e} = \left[\underbrace{2}_{\text{Exc}} - \underbrace{2F}_{\text{Hartree}} \right] \frac{e^2}{4\pi^2\hbar} \ln\left(\frac{k_B T \tau_{tr}}{\hbar}\right) = A(F) \frac{e^2}{2\pi^2\hbar} \ln\left(\frac{k_B T \tau_{tr}}{\hbar}\right) \tag{6.5}$$

where F is a measure of screening in the system: F vanishes for the case when electrostatic interaction are poorly screened, while in the case of strong screening F approaches unity and the corrections to the conductivity due to electron-electron interactions disappear. In our measurements, the residual temperature dependence in the WL-corrected conductivity (Figure 6.5b), suggest at the qualitative level that the interaction is not completely screened ($A \approx 0.758, 0.686$ for

[1] γ was obtained from the same temperature sweep measuring simultaneously $\rho_{xy}(T)$ and $\rho_{xy}(T)$. No difference was found when measuring $\rho_{xy}(T)$ and $\rho_{xy}(T)$ in independent temperature sweeps

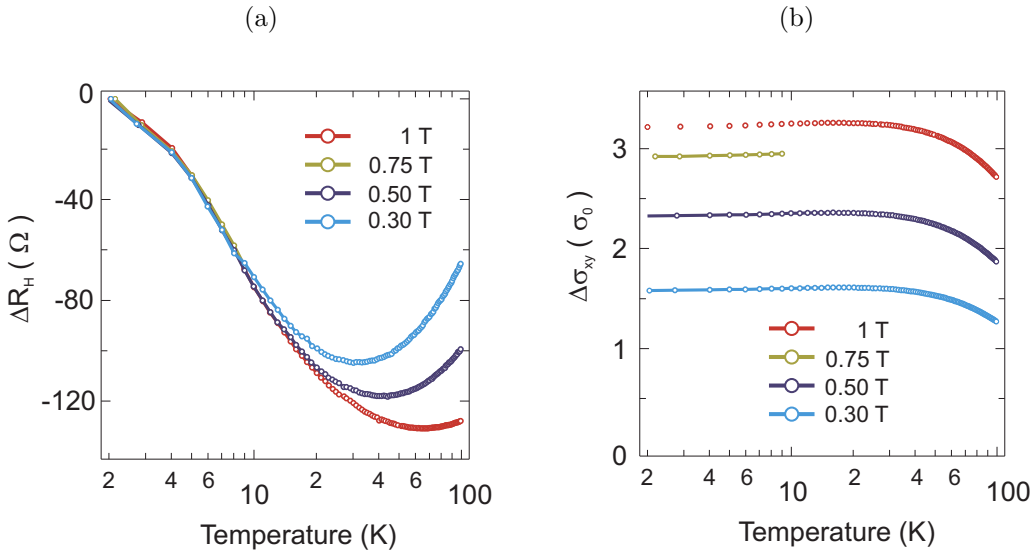

Figure 6.4: (a) The temperature dependence in the Hall coefficient does not arise from charge transfer, since the conductivity there is no such dependence and (b) quantification of the interaction strength from the residual T-dependence of conductivity once localization effects are subtracted.

samples S1 and S2 and therefore $F < 1$).

For graphene, a quantitative analysis needs to take into consideration interactions of electrons from different valleys. Accounting for this, a simplified expression for the prefactor A (eq.6.5) has been derived by Tikonenko et.al:

$$A_{Gr}(F) = 1 + c\left[1 - \frac{\ln(1+F)}{F}\right] \tag{6.6}$$

the expression $A_{Gr}(F)$ includes contributions from c "triplet" channels; it is argued that in graphene there exist 16 channels in total due to due to four-fold spin degeneracy of two interacting electrons and an additional four-fold degeneracy due to the two valleys. Out of this number, one resulting channel will be singlet, resulting in $c = 15$. Nevertheless, in the case of strong intervalley scattering c can be decreased, since channels with two electrons from different valleys give no contribution.

Comparison to other systems

Independently of the number of channels c, which implies some interpretation, the value of F for the SiC/G samples is within the limits $-0.18 \lesssim F \lesssim -0.04$, using $c = 3$ or 15 triplet channels. This value can be put into context by comparing to other "types" of graphene:

System	F
SiC/G (this work [56])	$-0.18 \lesssim F \lesssim -0.04$ ($c = 3$ or 15)
Hydrogenated graphene [71]	$-0.15 \lesssim F \lesssim -0.06$ ($c = 3$ or 7)
Exfoliated flakes [30]	$-0.13 \lesssim F \lesssim -0.08$ ($c = 7$)

For all practical purposes the numerical value of F is about the same for the different graphene systems, independently of the substrate. Its theoretical value has been calculated to be $F_{SiC} = -0.09$ [71] and $F_{flakes} = -0.10$ [30] (with relative dielectric constants $\kappa_{SiC} \approx 10$ and $\kappa_{SiO_2} \approx 4$). Its low magnitude has been explained to be a consequence of the chirality of the carriers, which reduce the angle for electron-electron scattering [30]. Thus, even though the dielectric constant of the substrate plays some role in screening the e-e interactions in graphene, our analysis has confirmed that the impact of a high-κ substrate is not all that determinant .

6.5 Summary

In summary, a comprehensive analysis of scattering processes in SiC/G in the quantum limit was presented. From the analysis of the weak localization it was found that in SiC/G the intravalley scattering (L_*), arising from long-range potentials, is comparable to the relaxation time ℓ; in combination with a larger intervalley scattering time L_i (short-range scatterers) we conclude that the conductivity SiC/G conductivity is limited by disorder created by donors in the buffer layer. Terraces on SiC are the proposed source of intervalley scattering.

Additionally, we were able to establish a spin relaxation of electrons at the time scale of ~ 50 ps, which we attribute to the presence of local magnetic momenta in/under graphene. The latter conclusion is driven from both the tendency

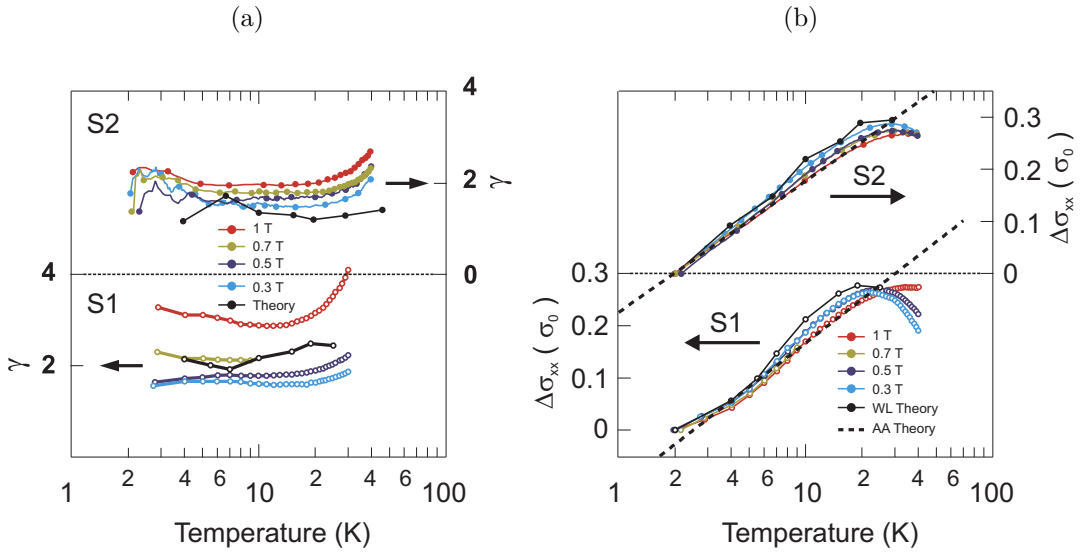

Figure 6.5: (a) The coefficient $\gamma = (\Delta R_H/R_H)/(\Delta R_{xx}/R_{rxx})$ suggest electron interactions are the remaining quantum correction to the conductivity of SiC after WL effects have been subtracted. (b) quantification of the interaction strength from the residual T-dependence of conductivity.

of the decoherence rate to saturate at the lowest temperatures and the experimental observation of L_ϕ to increase in the presence of an in-plane magnetic field.

Finally, the temperature dependence of the decoherence rate (τ_ϕ^{-1}) extracted from the WL analysis combined with the observed temperature dependence of γ, and the WL-corrected $\Delta\sigma_{xx}$ allow to identify electron interactions as a source of decoherence in the system. From the analysis of the e-e interaction correction, we conclude that the weak screening of interactions in SiC/G is determined by chirality of carriers to a greater extent, rather than due to the high dielectric constant of the substrate.

Chapter 7

Quantum Metrology with SiC/G

Metrology is the science and art of measuring, that is, comparing a physical quantity against a standard or reference. In the early days the measurement process was based on rudimentary techniques and references as arbitrary as the human body, but nowadays metrologists seek to develop universally valid standards based on fundamental physical constants, often employing sophisticated and complex techniques.

Universality, desired for a metrological standard, is found in quantum phenomena. In particular for the standard of electrical resistance, the Ohm (Ω), a two-dimensional material in the quantum Hall regime displays plateaux in the transversal resistance with values given by $R_K = h/\nu e^2$, with h the Planck constant, e the electron charge and ν the filling factor, making the quantum Hall effect (QHE) the system of choice to define the Ohm. The von Klitzing constant, named after the discoverer of QHE, is according to the latest definition equal to $R_K = 25,812.8074434(84)\ \Omega$ with an standard uncertainty of 3.2×10^{-10} [72].

This chapter describes how our knowledge of R_K and confidence in the universality of the QHE can be improved by using the half-integer QHE in SiC/G. By a direct comparison with the QHE in a GaAs heterostructure, the actual implementation of the resistance standard, it is found no difference in the constant $R_K/2$ to an uncertainty of 8.6 parts in 10^{11}. This comparison, the most strict universality test of the QHE up to now, was limited by the maximum current that can flow in the GaAs heterostructure before the breakdown of QHE in this material. The results suggest that graphene grown epitaxially on the silicon face

of SiC is a better implementation for the standard of electrical resistance and make quantum metrology the first application in which graphene outperforms conventional semiconductors.

7.1 The need for metrology

Originally born to facilitate commerce and trade, metrology has evolved throughout history hand-in-hand with science and technology. Responding to the need of scientist for means of comparing experimental results, system of standardized units were created and accepted by convention. Currently, the most widely adopted system is the International System of Units (SI, from French Système international d'units), with base units for length, mass, time, electric current, thermodynamic temperature, amount of substance, and luminous intensity; the remaining units can be *derived* from the base units.

Nowadays metrology attempts to fulfil the measurement needs of both society and scientists. *Applied* metrology is concerned with transferring standards and measurement techniques to society for purposes such as manufacture or fair trade, while *fundamental* metrology, of interest for this chapter, focuses on precise realization of units in physical experiments, as well as the development of universally valid standards and measurement techniques.

A note on uncertainty

When measuring a physical quantity, there is always a deviation of the measured value from the actual, true value. For that reason a measurement is always accompanied with error bars denoting the range of values that, with some probability, enclose the true value. This *uncertainty* is always tried to be minimized by metrologists.

The uncertainty of a measurement depends on both, its accuracy and its precision. Accuracy reflects how close a measurement is to the true value, while precision (also called reproducibility) is a measure of dispersion. Uncertainty can be quantified through the so-called *Type A* and *Type B* analyses. Type A analysis provides information about the precision of the measurement and consists

in collecting data without changing the measurement conditions; the outcome of such analysis is information about the mean and standard deviation, reflecting the reproducibility of a measurement. Systematic errors (which can produce precise but inaccurate measurements) can be eliminated through a Type B evaluation; this involves judgements based in i.e. accumulated expertise about equipment or technical specification of instruments. The total reported uncertainty is the combination of individual standard uncertainties obtained from the Type A and Type B analysis, using a standard method to combine variances, the so-called "root-sum-of-squares" (RSS) [73].

Quantum Metrology

The original standards of the SI included objects that were susceptible to changes due to influence from the environment. For instance, the international prototype of the kilogram (IPK), a cylinder composed of 90% platinum and 10% iridium, has been gaining weight at a rate of about 50 μg every 100 years; this metallic cylinder is clearly a poor embodiment of the mass standard.

The universality and timelessness needed for a standard is found in quantum-mechanical phenomena. An example of this is the time/frequency standard using an atomic clock, based on the radiation that atoms resonantly absorb; the caesium-based clock is expected to gain (or lose) one second in 100 million years [74, 75]. The definition of the volt through the inverse AC Josephson effect is another example; in a tunnel junction between two superconductors, radiation with frequency f will generate an additional superconducting current crossing the tunnel junction when the voltage across the barrier satisfies the relationship $V_{DC} = n(h/2e)f$, with n an integer, h the Planck constant, and e the electron charge. Used as a frequency-to-voltage converter with conversion ratio $h/2e = (1/483597.9)$ VGHz^{-1}, arrays of Josephson junctions are used in combination with the radiation referenced by the caesium-133 atomic clock to produce the volt standard.

7.2 Quantum Hall effect for electrical resistance standard

Until 1989, the unit of electrical resistance, the Ohm, was defined through technically complicated experiments using the A.C. resistance of a calculable capacitor, R=1/ωC, reaching uncertainties in the order of 10^{-7} [76].

With the discovery of the quantum Hall effect, observed exclusively in two-dimensional systems, it was immediately realized that a very precise and accurate value of resistance can be reproducibly obtained by measuring the voltage corresponding to any of the plateaux in the transversal voltage V_{xy}, given by

$$R_{xy} = \frac{V_{xy}}{I_{xx}} = \frac{h}{\nu e^2} = \frac{R_K}{\nu} \tag{7.1}$$

where h is the Planck constant, e the electron charge, and ν an integer.

The convenience and reproducibility of the QHE led to its establishment as the standard for electrical resistance since 1990. From technical point of view, measurement of the quantum Hall resistance, the ratio of two fundamental constants (h/e^2), reduces to measuring a voltage (V_{xy}) with high precision and accuracy. In practice, GaAs heterostructures are preferred because the 2D electron gas is easier to realize and the smaller effective mass(compare $m^*_{GaAs} = 0.067m_e$ to $m^*_{Si} = 0.26m_e$) result in a larger Landau level spacing.

An additional advantage from fundamental point of view is that the quantum Hall effect is considered to be a topological invariant, that means, it is not altered by the electron-electron interaction, spin-orbit coupling, hyperfine interaction with the nuclei or gravity or details of the sample (disorder) [77]. As a test of this hypothesis, the value of R_K has been tested in two different systems, namely Si MOSFET's and GaAs heterostructures, where R_K was found to be the same in both materials with an uncertainty of .3 parts in 10^9 [78, 79].

7.3 Why graphene?

Graphene is a truly two-dimensional material and thus provides a unique test bed for the universality of R_K, since prior implementations of two-dimensional systems

were in reality electrons confined at the interface of two materials. Additionally, the larger energy spacing between the first two Landau levels ($36 \times \sqrt{B}$ meV), compared with $1.7 \times B$ meV for GaAs-based systems, where B is the magnetic field in Tesla, allows the quantum Hall effect to be observed even at room temperature [80]. This is a big advantage for the development of a more practical resistance standard operating at a lower magnetic field or at higher temperature.

The first attempt of using graphene for metrology utilized an exfoliated flake; in this experiment a rather modest uncertainty of 15 parts in 10^6 was reported, a factor of 1,000 worse than values reported for GaAs. The cause of the high uncertainty was explained through the high contact resistance of the metal electrodes attached to the graphene and the low breakdown current in the sample; one possible reason for this was the small size of the sample ($\sim 10\mu\text{m}^2$).

Why SiC/G?

Following the example of exfoliated flakes, the initial motivation to use SiC/G was the large area and high quality of the as-grown graphene monolayers. Large area samples, it was reasoned, would allow to fabricate better ohmic contacts to the sample minimizing noise and Joule heating at high currents. Besides, fabrication of quantum hall arrays in SiC/G would reduce to a couple of microlithography steps.

During our studies it was indeed shown that low contact resistance can be achieved in SiC/G (in some cases $R_c \lesssim 1\ \Omega$) (Figure 7.1); the reason for this however, cannot be attributed entirely to the large area of the samples, and aspects such as contact material and carrier concentration in the graphene monolayer seem to play a role. Currently, we are performing experiments aiming to understand the origins if contact resistance to SiC/G. The best contact resistance at the moment is obtained with Ti/Au (5 nm /75 nm); surprisingly, the contact resistance can vary up to two orders of magnitude and the minimum coincides with the Dirac point.

Another advantage is the fact that the current needed to break down the QHE, denoted as critical current (i_c), was found to dynamically increase with increasing magnetic fields (Section 4.5), making SiC/G especially suitable for

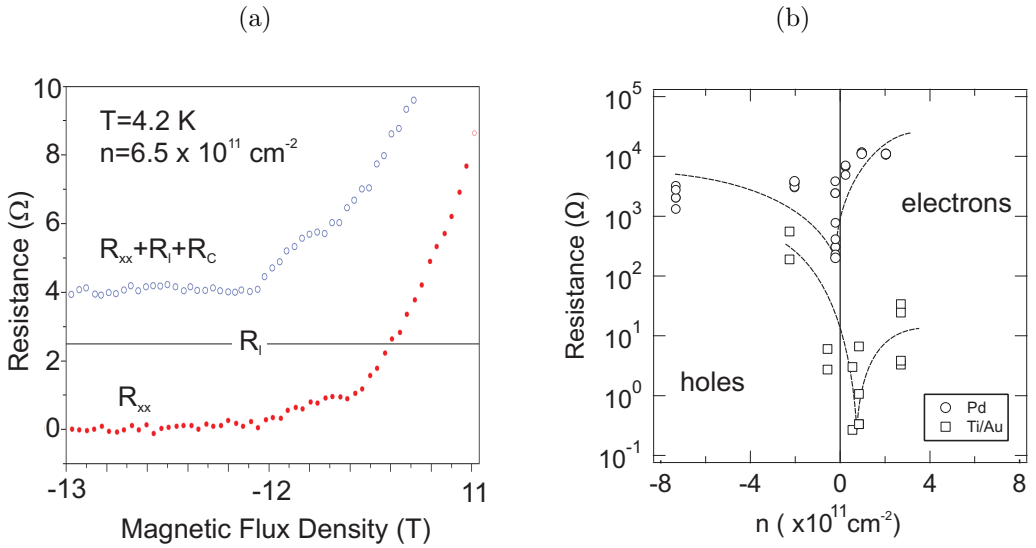

Figure 7.1: (a) Contact resistance (R_C) in a Hall bar measured in a three-point configuration in the quantum hall regime, when $\rho_{xx} \sim 0$; the contacts were fabricated using standard e-beam lithography and Ti/Au (5nm/75nm) were employed. (b) R_C is lower for Ti/Au than for Pd and strongly dependent on carrier concentration, varying over three orders of magnitude; interestingly, R_C reaches a minimum close to the Dirac point. For these measurements the contacts were evaporated through a shadow mask so that the metal/graphene interface is clean; the carrier concentration has been varied using a solid electrolyte and the contact resistance has been measured in a three-terminal configuration in the quantum Hall regime ($T = 2$ K).

QHE metrology compared to GaAs, exfoliated flakes or even epitaxial graphene on the carbon face of SiC. Large i_c (of the order of hundreds of μA) improve the signal-to-noise ratio in measurements and allow for higher uncertainties to be achieved. One reason for the observed large i_c is attributed to the magnetic field-dependent transfer of electrons from the substrate into SiC (Section 4.5), and another hypothesis is related to cooling of the hot spot (the point where electrons are injected into graphene) via emission of phonons into the bulk of SiC. Together with ohmic contacts to graphene, this will be a topic of future studies.

7.4 Quantum Metrology with SiC/G

Hall bars where fabricated according to Chapter 3 and the accuracy of the Hall resistance quantization was established by comparing R_{xy} in SiC/G with a calibrated (wire-wound) resistor, traceable to the GaAs quantum Hall resistance standard, using a cryogenic current comparator (CCC) bridge.

The initial attempt showed that $R_K/2$ in graphene was essentially the same to the established value of $h/2e^2$ with an uncertainty at the level of 3 parts in a billion (Figure 7.3a); this was a four orders of magnitude improvement on the result obtained for exfoliated graphene flakes. Compared to this latter, SiC/G samples benefited from a lower contact resistance ($\sim$ 1 Ω) and a higher probe current (11.6 μA), which leaded to a higher precision measurements of R_{xy} to a great extent due to an improved signal-to-noise ratio.

The origin of the observed uncertainty was analysed through the Allan deviation of R_{xy} as a function of measurement time; the fact that these data followed a $\propto t^{-1/2}$ dependence indicates that the predominant source of uncertainty is white (uncorrelated random) noise. This suggested that this result could be further improved by measuring for longer times or by increasing somehow the critical current in the Hall bars.

From technical point of view it would be an advantage to be able to work at $T = 4.2$ K. The robustness of the QHE in SiC/G against temperature was tested by measuring at this temperature and it was found that the critical current decreased to a few μA. Measuring at lower currents means lower signal-to-noise ratio and therefore the uncertainty of the data accumulated over a comparable time interval was higher. Hence, at this stage it was possible to have a quantum resistance standard operating at the liquid helium temperature, but the performance was enhanced at $T = 300$ mK.

Improving the sample

A requisite for any metrological standard is its temporal stability. In order to avoid stochastic doping of graphene from the ambient (occurring after a few thermal cycles), the samples were protected by encapsulation with organic polymers, known to be harmless for the mobility of graphene, as described in Chapter 5.

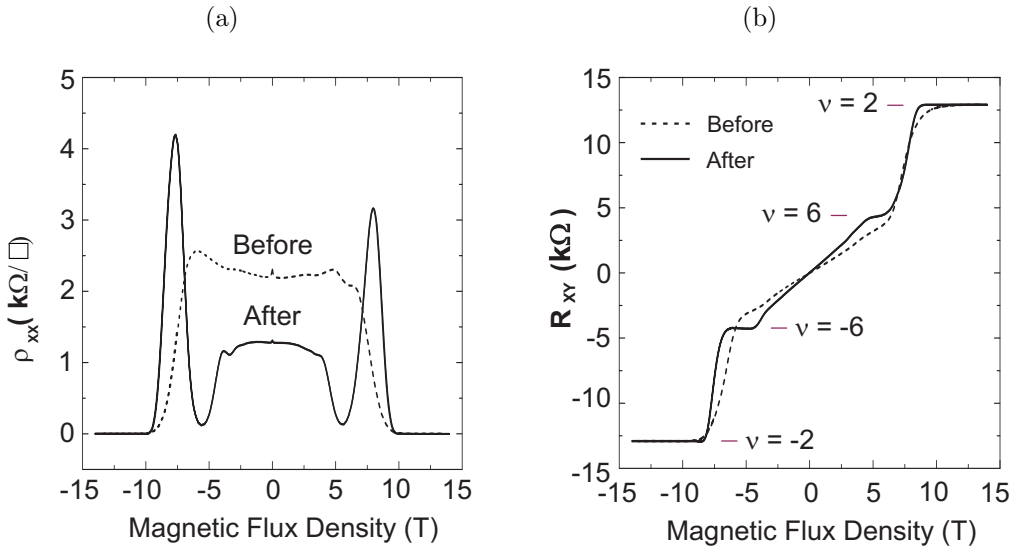

Figure 7.2: Encapsulation and photochemical gating resulted in a more homogeneous sample as noted by (a) a flat $\rho_{xx}(B)$ and (b) sharper plateaux in $\rho_{xy}(B)$.

Additionally, the carrier concentration of the sample was controlled using photochemical gating by exposure to Deep UV and once the carrier concentration was fixed the effect was observed to last for long periods (∼years) (specially if the sample is protected from any light source). In fact, after 12 thermal cycles over 2 years, the electron concentration in graphene only changed by 3% (decreased).

Encapsulation and photochemical gating resulted in a significantly more uniform doping profile throughout the sample as revealed by a flat ρ_{xx} background near zero field instead of a parabolic background in the untreated sample, significantly enhanced Shubnikov-de Haas oscillations of ρ_{xx} and sharper quantum Hall plateaux corresponding to $\nu = 2, 6$ (Figure 7.2).

As a consequence of a more homogeneous sample after encapsulation and photochemical gating, the breakdown current increased about 50 times from 10 to 500 μA; large currents in these samples facilitated measurements an order of magnitude more precise compared to the uncoated sample (0.3 parts in a billion).

7.5 Comparison of SiC/G and GaAs Heterostructure

The uncertainties described in the previous sections were obtained by comparing SiC/G with a transfer resistor, that is, a resistor that has been calibrated with a GaAs heterostructure. In order to eliminate any possible systematic error, a direct comparison between SiC/G and the GaAs heterostructures was performed.

Direct comparison of the quantum Hall effect in graphene and that in a conventional 2D gas is perhaps the most strict test of universality ever performed. Previous comparison between the QHE in the 2D gas formed in GaAs and Silicon MOSFET's showed uncertainties at the level of 0.3 parts in 10^9. In that case however, GaAs and Si are similar in the sense that the two-dimensional systems is achieved by confining electrons at interfaces of semiconductors with a parabolic band structure, while graphene on the other hand is a true two-dimensional material, with a linear energy dispersion.

For the comparison of encapsulated SiC/G against two GaAs/AlGaAs samples 4 cryostats were employed: 1 for the SiC sample, 1 for the GaAs samples, 1 for the CCC bridge and 1 for null-detector (REF). The graphene sample was held at $T = 300$ mK and $B = 14$ T, while both GaAs devices were placed in system at $T = 1.5$ K and either $B = 9.5$ T (device 1) or 10.5 T (device 2). The resistance of graphene was compared to that of the GaAs device in a null measurement using CCC bridge described in Chapter 3.

The outcome of this comparison is that the Hall resistance is quantized to the same value in both GaAs and SiC/G with an uncertainty of 8.6×10^{-11} (0.086 parts per billion). This suggest that this value is fundamentally material independent and give there is no correction to the quantity $h/2e^2$. The direct comparison of GaAs and SiC/G represents a factor of 35 improvement on the initial attempt obtained using the unprotected sample and the transfer resistor (REF) (Figure 7.3b). The uncertainty of the comparison was limited by the maximum source-drain current that the GaAs device can sustain without dissipation ($\sim 100 - 150$ μA) compared to $i_c = 500$ μA in the graphene sample.

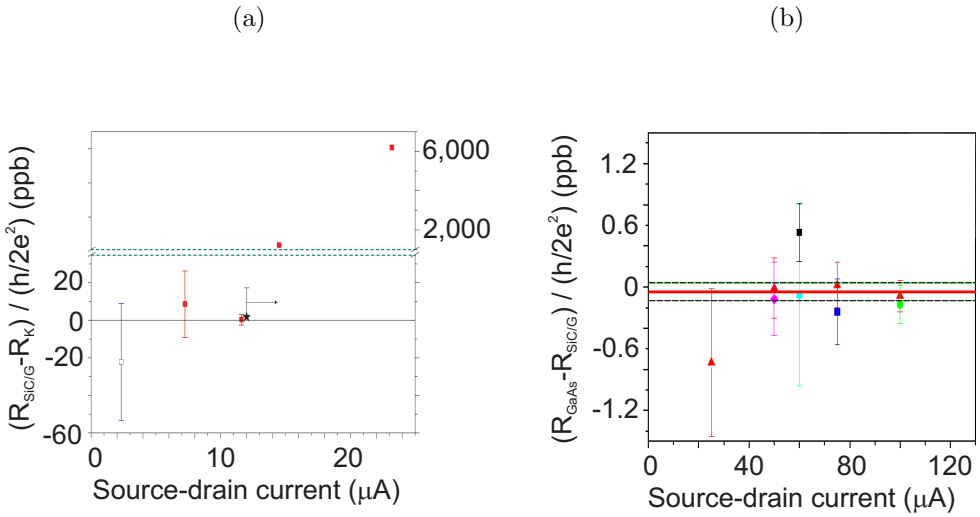

Figure 7.3: (a) Uncertainties achieved in the initial attempt with the uncoated sample and (b) the improvement of a factor of 35 in a direct comparison of encapsulated SIC/G with a GaAs heterostructure; the comparison was limited by the critical current i_c in the GaAs heterostructure, 4 times smaller than the critical current of the SiC/G sample.

7.6 Summary

The half-integer quantum Hall effect in SiC/G as the standard of the electrical resistance has been introduced. A direct comparison with the QHE in GaAs supports the hypothesis that the electrical resistance is quantized in units of h/e^2; from fundamental and technical reasons SiC/G outperforms GaAs/AlGaA as quantum resistance standard:

- The half-integer quantum Hall effect in epitaxial graphene on SiC is precise to higher temperatures due to the larger spacing between the $N = 0$ and $N = 1$ Landau levels.

- The higher source-drain currents observed in SiC/G result in higher signal-to-noise ratio compared to GaAs, which allows performing measurements with less uncertainty. High critical current are related to the magnetic field dependent charge transfer from the substrate into graphene.

Future work will concentrate in investigating the origin of high critical currents and low contact resistance to SiC/G. Additionally, optimization of the SiC/G Hall bars in terms of geometry will be sought, as well as the fabrication of parallel/series arrays of Hall bars that produce standard values of resistances lower than h/e^2 (i.e. 100 Ω).

Chapter 8

Summary & Outlook

Growth of epitaxial graphene on silicon carbide (SiC/G)

This work described how graphene grown epitaxially on the silicon face of 4H silicon carbide was characterized through low temperature magnetotransport; in collaboration with the group of Rosie Yakimova, growth at high temperature (T = 2000 ^{o}C) and pressure (1 atm of Argon) were identified as the suitable growth conditions obtaining a single layer of graphene. Despite the defects on the substrate such as terraces, the half-integer quantum Hall effect observed in large Hall bars (about 200 μm long) suggest that the graphene layer is continuous over the terraces. Future growth-related work will be aimed at reducing the formation of terraces, increasing further the crystal domain size and also to produce monolayers with doping levels below the currently observed 1-10 $\times 10^{12}$ cm^{-2} (and in this way increase further carrier mobilities).

Carrier density control in SiC/G

The as-grown doping levels in the graphene layer, a consequence of the interaction with the substrate and donors in the buffer layer produced during growth, could be experimentally adjusted using: a) electrostatic gating using organic dielectrics, b) photochemical gating or c) solid electrolytes, at levels n$\sim 10^{11}$, $\sim 10^{12}$ and $\sim 10^{13}$ cm^{-2} respectively. The preferred method was photochemical gating, as it does not degrade the mobility of the sample and it is a non-volatile effect; however, this method is only useful when the initial concentration of the as-

grown graphene is of the order of n$\sim 10^{12}$ cm^{-2}. Despite having found a solid electrolyte that does not degrade graphene, its use is limited by the requirement that gating is only possible when the temperature of the sample is > 220 K; this implies the sample has to be warmed-up every time the carrier concentration has to be tuned and this translates into time-consuming measurements. We are still seeking novel gating schemes that allow to control the carrier density in graphene at low temperatures, while still preserving the carrier mobility of the pristine sample.

SiC/G-based sensors

The photo-chemically gateable heterostructure used to control the carrier concentration in graphene can be used in the future as a prototypical architecture for the development of graphene-based sensors, using a spacer layer directly in contact with graphene that protects its integrity, followed by a layer that responds to a given stimulus. The sensitivity of graphene to changes in its carrier concentration (manifested via its resistivity) combined with the vast possibilities offered by polymer engineering suggest that virtually any type of sensor can be developed using epitaxial graphene.

Fine details of scattering in SiC/G

In the analysis of quantum corrections to the conductivity of SiC/G two contributions were decoupled and quantified: the weak localization correction (WL), due to interference of electron waves, and the correction arising from electron-electon interaction (E-E), enhanced due to disorder and poor electrostatic screening in this material. From the analysis of the WL analysis it was found that scattering in SiC/G is limited by charged impurities present in the buffer layer, which introduce disorder that breaks the symmetry of the graphene lattice; intervalley scattering has been systematically observed in all the fabricated samples and a suggested explanation is the presence of terraces on the substrate; the extracted temperature dependence of the decoherence rate allowed to suggest: 1) the observed residual decoherence at the lowest temperature is due to the presence of

magnetic impurities in the system and 2) at higher temperatures the decoherence is due to electron-electron interaction. From the analysis of the E-E interaction, it was concluded that the high relative permittivity of the silicon carbide substrate does not modify the local electrostatic environment of interacting electrons.

Spintronics

The analysis of WL provided an indirect measurement of the spin relaxation time in SiC/G, at the level of 50 ps, and possibly limited by magnetic impurities. Future work will be focused in confirming the presence of such magnetic impurities and understanding its origin: in the best case scenario these are introduced during fabrication (and thus can be avoided), otherwise these are intrinsically present in SiC/G and could be due to defects in the monolayer (dangling bonds are thought to be magnetic). Preliminary results show that applying a magnetic field in the plane of the graphene layer increases the decoherence length by 50%, supporting so far the hypothesis of magnetic impurities (REF Ed macan). The understanding of spin relaxation mechanism in this material is crucial for future spintronics applications.

Quantum Metrology

It was shown that the half-integer quantum Hall effect in SiC/G is a superior standard for electrical resistance, compared to the conventional quantum Hall effect observed in GaAs heterostructures. A direct comparison with the QHE in GaAs, the most strict universality test of the QHE ever performed, supports the hypothesis that the electrical resistance is quantized in units of h/e^2. The comparison was limited by the highest current that can flow without dissipation in the GaAs sample, being 4 times lower than in the SiC/G sample. Future work will concentrate in investigating the origin of high critical currents and low contact resistance to SiC/G, and the fabrication of parallel/ series arrays of Hall bars that produce standard values of resistances (i.e. 100 Ω).

Appendix A:Sample Preparation

Lithography Steps

1) Anchors (feature size $> 100\mu$m)

- Spin-coat 350 nm copolymer resist [poly(methylmethacrylate- co -methacrylate acid)] diluted in ethyl lactate (10% w/w)(MicroChem Corp.); bake at 160 °C on hotplate for 5 min.
- Spin-coat 300 nm ZEP520A (Nippon Zeon Co., Ltd); bake at 160 °C on hotplate for 5 min.
- Pattern with electron beam, 100 keV (JEOL JBX9300FS).
- Develop ZEP520A (top layer) in o-Xylene for 20 seconds, rinse in Isopropanol, blow dry with N_2
- Develop copolymer (bottom layer) in IPA/H_2O ($93\% : 7\% v/v$) for 1 minute 30 seconds (de-ionized water); rinse in Isopropanol; blow dry with N_2
- Remove graphene with oxygen plasma for 1 min; 50 W of RF power, 250 mbar and 10 sccm of O_2
- Evaporate titanium, 5 nm, with rate 2 $\mathring{A}/s$+Evaporate gold, $70 - 150$ nm, with rate 4 $\mathring{A}/s$.
- Lift-off in acetone, overnight; rinse in isopropanol; blow dry N_2.

2) Ohmic Contacts (feature size > 100 μm)

- Spin-coat 350 nm copolymer resist; bake at 160 °C on hotplate for 5 min.
- Spin-coat 300 nm ZEP520A; bake at 160 °C on hotplate for 5 min.

- Pattern with electron beam.
- Develop ZEP520A (top layer) in o-Xylene for 20 seconds, rinse in Isopropanol, blow dry with N_2
- Develop copolymer (bottom layer) in IPA/H_2O (93% : 7%v/v) for 2 minute; rinse in Isopropanol twice; blow dry with N_2
- Evaporate titanium, 5 nm, rate 2 $\mathring{A}/s$ + gold, $70-150$ nm, rate 4 $\mathring{A}/s$.
- Lift-off in acetone, overnight; rinse in isopropanol; blow dry N_2.

3) Defining Hall bars (minimum feature size 1μm)

- Spin-coat 100 nm copolymer resist; bake at 160 °C on hotplate for 5 min.
- Spin-coat 300 nm ZEP520A; bake at 160 °C on hotplate for 5 min.
- Pattern with electron beam.
- Develop ZEP520A (top layer) in o-Xylene for 20 seconds, rinse in Isopropanol, blow dry with N_2
- Develop copolymer (bottom layer) in IPA/H_2O (93% : 7%v/v) for 1 minute 30 seconds; rinse in Isopropanol; blow dry with N_2
- Remove graphene with oxygen plasma for 1 min: 50 W of RF power, 250 mbar and 10 sccm of O_2
- Check in probe station that 1) the Hall bars are conducting and 2) neighboring Hall bars are electrically isolated.
- Lift-off in acetone, overnight; rinse in isopropanol; blow dry N_2.

Encapsulation and photochemical gating

- Spin-coat >50 nm (standard thickness used was 100 nm) copolymer resist [poly(methylmethacrylate- co -methacrylate acid)] diluted in ethyl lactate (10% w/w)(MicroChem Corp.); bake at 170 °C on hotplate for 5 min.
- Spin-coat 300 nm ZEP520A (Nippon Zeon Co., Ltd); bake at 170 °C on hotplate for 5 min; optionally add a second layer of 300 nm ZEP520A (bake again).
- Expose to Deep UV (Zeiss) in intervals of 20 sec and measure carrier concentration at each step until the desired concentration is achieved.

Solid electrolyte

- First, dilute polyethylene oxide (M_v=200,000g/mol, Sigma-Aldrich) in acetonitrile to 3 wt %.
- Mix the solution with lithium trifluoromethanesulfonate (CF_3SO_3Li, Sigma-Aldrich, 99.995% trace metals basis) to give a ratio 16:1 ratio of Oxygen/Li.
- Ultrasound for 10 min
- When spin -coating the chip, filter though a 200 nm poly(tetrafluoroethylene) (PTFE) syringe filter.
- Spin-coat at 3000 rpm, 1 min
- Bake at 85 ^{o}C for 5 min on hotplate

. APPENDIX A:SAMPLE PREPARATION

Acknowledgements

It has been a privilege to work under supervision of Andrey and Sergey. Working in the lab with them is really fun.

I am very grateful to many people who contributed directly or indirectly to this thesis :

Alex and Avgust, when I started invading their lab; our little group, Tom, Arseniy, Karin and Sebastian; JT and Sasha Tzalenchuk at NPL, who has been like a third supervisor, in many aspects; Rositza and Mikael, who provided the nice samples for our experiments; Sergey Kopilov and Vladimir Fal'ko; Kasper and Tina, our great chemical team; Tord Claeson, providing always very valuable input; Tomas Lofwander for reading the manuscript, together with Dr. Schneiderman (semicolon); and Fredrik, Thilo, Martin and Justin, who always provide enlightening discussions.

Agradecimientos especiales...

...a mis familia, mis Papás, a la Gordis y a Malenis. (Tanto!)

References

[1] K S Novoselov, A K Geim, S V Morozov, D Jiang, Y Zhang, S V Dubonos, I V Grigorieva, and a a Firsov. Electric field effect in atomically thin carbon films. *Science*, 306(5696): 666–9, 2004.

[2] K S Novoselov, A K Geim, S V Morozov, D Jiang, M I Katsnelson, I V Grigorieva, S V Dubonos, and a a Firsov. Two-dimensional gas of massless Dirac fermions in graphene. *Nature*, 438(7065):197–200, 2005.

[3] PR Wallace. The band theory of graphite. *Physical Review*, 329, 1947.

[4] Y-M Lin, C Dimitrakopoulos, K A Jenkins, D B Farmer, H-Y Chiu, A Grill, and Ph Avouris. 100-GHz transistors from wafer-scale epitaxial graphene. *Science*, 327(5966): 662, 2010.

[5] Yu-Ming Lin, Alberto Valdes-Garcia, Shu-Jen Han, Damon B Farmer, Inanc Meric, Yanning Sun, Yanqing Wu, Christos Dimitrakopoulos, Alfred Grill, Phaedon Avouris, and Keith A Jenkins. Wafer-scale graphene integrated circuit. *Science*, 332(6035):1294–7, 2011.

[6] R. R. Nair, P. Blake, A. N. Grigorenko, K. S. Novoselov, T. J. Booth, T. Stauber, N. M. R. Peres, and A. K. Geim. Fine structure constant defines visual transparency of graphene. *Science*, 320(5881):1308, 2008.

[7] Claire Berger, Zhimin Song, Tianbo Li, Xuebin Li, Asmerom Y Ogbazghi, Rui Feng, Zhenting Dai, Alexei N Marchenkov, Edward H Conrad, Phillip N First, and Walt A De Heer Heer. Ultrathin epitaxial graphite : 2d electron gas properties and a route toward graphene-based nanoelectronics. *J. Phys. Chem. B*, pages 19912–19916, 2004.

[8] Taisuke Ohta, Aaron Bostwick, Thomas Seyller, Karsten Horn, and Eli Rotenberg. Controlling the electronic structure of bilayer graphene. *Science*, 313(5789):951–4, 2006.

[9] J. Hass, R. Feng, T. Li, X. Li, Z. Zong, W. A. de Heer, P. N. First, E. H. Conrad, C. A. Jeffrey, and C. Berger. Highly ordered graphene for two dimensional electronics. *Applied Physics Letters*, 89(14):143106, 2006.

[10] Claire Berger, Zhimin Song, Xuebin Li, Xiaosong Wu, Nate Brown, Cécile Naud, Didier Mayou, Tianbo Li, Joanna Hass, Alexei N Marchenkov, Edward H Conrad, Phillip N First, and Walt A de Heer. Electronic confinement and coherence in patterned epitaxial graphene. *Science*, 312(5777):1191–6, 2006.

[11] C. Virojanadara, M. Syväjarvi, R. Yakimova, L. Johansson, A. Zakharov, and T. Balasubramanian. Homogeneous large-area graphene layer growth on 6H-SiC(0001). *Physical Review B*, 78(24), 2008.

[12] Samuel Lara-Avila, Alexei Kalaboukhov, Sara Paolillo, Mikael Syväjärvi, Rositza Yakimova, Vladimir Fal'ko, Alexander Tzalenchuk, and Sergey Kubatkin. SiC Graphene Suitable For Quantum Hall Resistance Metrology. *arXiv:0909.1193v1*, 2009.

[13] Alexander Tzalenchuk, Samuel Lara-Avila, Alexei Kalaboukhov, Sara Paolillo, Mikael Syväjärvi, Rositza Yakimova, Olga Kazakova, T J B M Janssen, Vladimir Fal'ko, and Sergey Kubatkin. Towards a quantum resistance standard based on epitaxial graphene. *Nature nanotechnology*, 5(3):186–9, 2010.

[14] T. Shen, J. J. Gu, M. Xu, Y. Q. Wu, M. L. Bolen, M. A. Capano, L. W. Engel, and P. D. Ye. Observation of quantum-Hall effect in gated epitaxial graphene grown on SiC (0001). *Applied Physics Letters*, 95(17):172105, 2009.

[15] Xiaosong Wu, Yike Hu, Ming Ruan, Nerasoa K Madiomanana, John Hankinson, Mike Sprinkle, Claire Berger, and Walt A. de Heer. Half integer quantum Hall effect in high mobility single layer epitaxial graphene. *Applied Physics Letters*, 95(22):223108, 2009.

[16] Johannes Jobst, Daniel Waldmann, Florian Speck, Roland Hirner, Duncan K. Maude, Thomas Seyller, and Heiko B. Weber. Quantum oscillations and quantum Hall effect in epitaxial graphene. *Physical Review B*, 81(19), 2010.

[17] K. v. Klitzing, G. Dorda, and M. Pepper. New method for high-accuracy determination of the fine-structure constant based on quantized hall resistance. *Physical Review Letters*, 45:494–497, 1980.

[18] S. Datta. *Electronic Transport in Mesoscopic Systems*. Cambridge Studies in Semiconductor Physics and Microelectronic Engineering. Cambridge University Press, 1997.

[19] G. Bergmann. Physical interpretation of weak localization: A time-of-flight experiment with conduction electrons. , 28:2914–2920, 1983.

[20] Gerd Bergmann. Weak localization in thin films: a time-of-flight experiment with conduction electrons. *Physics Reports*, 107(1):1 – 58, 1984.

[21] Gerd Bergman. Influence of spin-orbit coupling on weak localization. *Physical Review Letters*, 48:1046–1049, 1982.

[22] S. Datta. *Quantum Transport: Atom To Transistor*. Cambridge University Press, 2005.

[23] Aaron Bostwick, Taisuke Ohta, Thomas Seyller, Karsten Horn, and Eli Rotenberg. Quasiparticle dynamics in graphene. *Nature Physics*, 3(1):36–40, 2007.

[24] a. Castro Neto, F. Guinea, N. Peres, K. Novoselov, and A. Geim. The electronic properties of graphene. *Reviews of Modern Physics*, 81(1):109–162, 2009.

[25] V. P. Gusynin and S. G. Sharapov. Unconventional integer quantum hall effect in graphene. *Physical Review Letters*, 95:146801, 2005.

[26] A K Geim and K S Novoselov. The rise of graphene. *Nature materials*, 6(3):183–91, 2007.

[27] I. L. Aleiner and K. B. Efetov. Effect of disorder on transport in graphene. *Physical Review Letters*, 97:236801, 2006.

[28] A. F. Morpurgo and F. Guinea. Intervalley scattering, long-range disorder, and effective time-reversal symmetry breaking in graphene. *Phys. Rev. Lett.*, 97:196804, 2006.

[29] E. McCann, K. Kechedzhi, Vladimir Fal'ko, H. Suzuura, T. Ando, and B. Altshuler. Weak-Localization Magnetoresistance and Valley Symmetry in Graphene. *Physical Review Letters*, 97(14):14–17, 2006.

[30] F. V. Tikhonenko, a. a. Kozikov, a. K. Savchenko, and R. V. Gorbachev. Transition between Electron Localization and Antilocalization in Graphene. *Physical Review Letters*, 103(22):1–4, 2009.

[31] John M. Martinis, Michel H. Devoret, and John Clarke. Experimental tests for the quantum behavior of a macroscopic degree of freedom: The phase difference across a josephson junction. *Physical Review B*, 35:4682–4698, 1987.

[32] K. Bladh, D. Gunnarsson, E. Hürfeld, S. Devi, C. Kristoffersson, B. Smålander, S. Pehrson, T. Claeson, P. Delsing, and M. Taslakov. Comparison of cryogenic filters for use in single electronics experiments. *Review of Scientific Instruments*, 74(3):1323, 2003.

[33] T. Bauch, F. Lombardi, F. Tafuri, A. Barone, G. Rotoli, P. Delsing, and T. Claeson. Macroscopic quantum tunneling in d-wave $YBa_2Cu_3o_{7-\delta}$ josephson junctions. *Physical Review Letters*, 94:087003, 2005.

[34] B. Douçot. *The Quantum Hall effect: Poincaré Seminar 2004*. Progress in mathematical physics. Birkhäuser Verlag, 2005.

[35] I. K. Harvey. A precise low temperature dc ratio transformer. *Review of Scientific Instruments*, 43(11):1626–1629, 1972.

[36] Johann Coraux, Alpha T. N'Diaye, Martin Engler, Carsten Busse, Dirk Wall, Niemma Buckanie, Frank-j Meyer Zu Heringdorf, Raoul van Gastel, Bene Poelsema, and Thomas Michely. Growth of graphene on Ir(111). *NEW JOURNAL OF PHYSICS*, 11, 2009.

[37] Dacheng Wei, Yunqi Liu, Yu Wang, Hongliang Zhang, Liping Huang, and Gui Yu. Synthesis of N-Doped Graphene by Chemical Vapor Deposition and Its Electrical Properties. *Nano Letters*, 9(5):1752–1758, 2009.

[38] Alpha T N'Diaye, Martin Engler, Carsten Busse, Dirk Wall, Niemma Buckanie, Frank-J Meyer zu Heringdorf, Raoul van Gastel, Bene Poelsema, and Thomas Michely. Growth of graphene on Ir(111). *New Journal of Physics*, 11(2):023006, 2009.

[39] Xuesong Li, Weiwei Cai, Jinho An, Seyoung Kim, Junghyo Nah, Dongxing Yang, Richard Piner, Aruna Velamakanni, Inhwa Jung, Emanuel Tutuc, Sanjay K Banerjee, Luigi Colombo, and Rodney S Ruoff. Large-area synthesis of high-quality and uniform graphene films on copper foils. *Science*, 324(5932):1312, 2009.

[40] Alfonso Reina, Xiaoting Jia, John Ho, Daniel Nezich, Hyungbin Son, Vladimir Bulovic, Mildred S Dresselhaus, and Jing Kong. Large area, few-layer graphene films on arbitrary substrates by chemical vapor deposition. *Nano letters*, 9(1):30, 2009.

[41] R. Cheung. *Silicon Carbide Microelectromechanical Systems for Harsh Environments*. Imperial College Press, 2006.

[42] J. Hass, F. Varchon, J. E. Millan-Otoya, M. Sprinkle, N. Sharma, W. A. De Heer, C. Berger, P. N. First, L. Magaud, and E. H. Conrad. Why multilayer graphene on 4H-SiC(000(1)overbar) behaves like a single sheet of graphene. *PHYSICAL REVIEW LETTERS*, 100(12), 2008.

[43] Francois Varchon, Pierre Mallet, Laurence Magaud, and Jean-Yves Veuillen. Rotational disorder in few-layer graphene films on 6H-SiC(000-1): A scanning tunneling microscopy study. *Physical Review B*, 77(16), 2008.

[44] Xiaosong Wu, Xuebin Li, Zhimin Song, Claire Berger, and Walt a. de Heer. Weak Antilocalization in Epitaxial Graphene: Evidence for Chiral Electrons. *Physical Review Letters*, 98(13):2–5, 2007.

[45] Pierre Darancet, Nicolas Wipf, Claire Berger, Walt A. de Heer, and Didier Mayou. Quenching of the quantum hall effect in multilayered epitaxial graphene: The role of undoped planes. *Physical Review Letters.*, 101:116806, 2008.

[46] Peter Sutter. Epitaxial graphene: How silicon leaves the scene. *Nature Materials*, 8(3): 171–172, 2009.

[47] Wataru Norimatsu and Michiko Kusunoki. Transitional structures of the interface between graphene and 6H–SiC (0001). *Chemical Physics Letters*, 468(1-3):52–56, 2009.

[48] Wataru Norimatsu and Michiko Kusunoki. Transmission Electron Microscope Observation of Interface Structures of Graphene on 6H-SiC. *Journal of Nanoscience and Nanotechnology*, 10(6):3884–3889, 2010.

[49] Luxmi, N. Srivastava, Guowei He, R. M. Feenstra, and P. J. Fisher. Comparison of graphene formation on c-face and si-face sic 0001 surfaces. *Physical Review B*, 82:235406, 2010.

[50] C. Riedl, C. Coletti, T. Iwasaki, A. A. Zakharov, and U. Starke. Quasi-free-standing epitaxial graphene on sic obtained by hydrogen intercalation. *Physical Review Letters*, 103:246804, 2009.

[51] P. Lauffer, K. V. Emtsev, R. Graupner, Th. Seyller, L. Ley, S. A. Reshanov, and H. B. Weber. Atomic and electronic structure of few-layer graphene on sic(0001) studied with scanning tunneling microscopy and spectroscopy. *Physical Review B*, 77:155426, 2008.

[52] Dong Sun, Zong-Kwei Wu, Charles Divin, Xuebin Li, Claire Berger, Walt A. de Heer, Phillip N. First, and Theodore B. Norris. Ultrafast relaxation of excited dirac fermions in epitaxial graphene using optical differential transmission spectroscopy. *Physical Review Letters*, 101:157402, 2008.

[53] Sergey Kopylov, Alexander Tzalenchuk, Sergey Kubatkin, and Vladimir I. Fal'ko. Charge transfer between epitaxial graphene and silicon carbide. *Applied Physics Letters*, 97(11): 112109, 2010.

[54] T. Janssen, A. Tzalenchuk, R. Yakimova, S. Kubatkin, S. Lara-Avila, S. Kopylov, and V. Falko. Anomalously strong pinning of the filling factor ν=2 in epitaxial graphene. *Physical Review B*, 83(23), 2011.

[55] F Schedin, A Geim, S Morozov, E Hill, P Blake, M Katsnelson, and K Novoselov. Detection of individual gas molecules adsorbed on graphene. *Nature Materials*, 6(9):652–655, 2007.

[56] Samuel Lara-Avila, Kasper Moth-Poulsen, Rositza Yakimova, Thomas Bjø rnholm, Vladimir Fal'ko, Alexander Tzalenchuk, and Sergey Kubatkin. Non-Volatile Photochemical Gating of an Epitaxial Graphene/Polymer Heterostructure. *Advanced Materials*, pages 878–882, 2011.

[57] Daniel Waldmann, Johannes Jobst, Florian Speck, Thomas Seyller, Michael Krieger, and Heiko Weber. Bottom-gated epitaxial graphene. *Nature Materials*, 10(5):357–360, 2011.

[58] J. R. Williams, L. DiCarlo, and C. M. Marcus. Quantum hall effect in a gate-controlled p-n junction of graphene. *Science*, 317(5838):638–641, 2007.

[59] Yu-Ming Lin, Keith a Jenkins, Alberto Valdes-Garcia, Joshua P Small, Damon B Farmer, and Phaedon Avouris. Operation of graphene transistors at gigahertz frequencies. *Nano letters*, 9(1):422–6, 2009.

[60] W. L. Kalb, T. Mathis, S. Haas, a. F. Stassen, and B. Batlogg. Organic small molecule field-effect transistors with Cytop^{TM} gate dielectric: Eliminating gate bias stress effects. *Applied Physics Letters*, 90(9):092104, 2007.

[61] J. Boland, Y. Suzuki, and Y.C. Tai. Micro electret power generator. In *The Sixteenth Annual International Conference on Micro Electro Mechanical Systems, 2003. MEMS-03 Kyoto. IEEE*, pages 538–541. IEEE.

[62] a. Facchetti, M.-H. Yoon, and T. J. Marks. Gate Dielectrics for Organic Field-Effect Transistors: New Opportunities for Organic Electronics. *Advanced Materials*, 17(14):1705–1725, 2005.

[63] Dmitri K. Efetov and Philip Kim. *Physical Review Letters, Pages = 256805, Title = Controlling Electron-Phonon Interactions in Graphene at Ultrahigh Carrier Densities, Volume = 105, Year = 2010.*

[64] B. Altshuler and A. Aronov. Electron-electron interactions in disordered systems. *series edited by AL Efros and M. Pollak*, 1985.

[65] F. V. Tikhonenko, D. W. Horsell, R. V. Gorbachev, and A. K. Savchenko. Weak Localization in Graphene Flakes. *Physical Review Letters*, 100(5):056802, 2008.

[66] YC Ma, PO Lehtinen, AS Foster, and RM Nieminen. Magnetic properties of vacancies in graphene and single-walled carbon nanotubes. *New Journal of Physics*, 6, 2004.

[67] Oleg V. Yazyev and Lothar Helm. Defect-induced magnetism in graphene. *Physical Review B*, 75(12), 2007.

[68] Oleg V. Yazyev. Magnetism in disordered graphene and irradiated graphite. *Physical Review Letters*, 101(3), 2008.

[69] Edward McCann and Vladimir I. Fal'ko. z→-z symmetry of spin-orbit coupling and weak localization in graphene. *Physical Review Letters*, 108:166606, 2012.

[70] H. Fukuyama. Hall Effect in Two-Dimensional Disordered Systems. *J. Phys. Soc. Japan*, 49(2):644–648, 1980.

[71] Johannes Jobst, Daniel Waldmann, Igor V. Gornyi, Alexander D. Mirlin, and Heiko B. Weber. Electron-electron interaction in the magnetoresistance of graphene. *Physical Review Letters*, 108:106601, 2012.

[72] CODATA Recommended Values of the Fundamental Physical Constants: 2010. page 94, 2012.

[73] S. D. Phillips, K. Eberhardt, and B Parry. Guidelines for Expressing the Uncertainty of Measurement Results Containing Uncorrected Bias. *Journal of Research of the National Institute of Standards and Technology*, 102(5), 1997.

[74] W. H. Oskay, S. A. Diddams, E. A. Donley, T. M. Fortier, T. P. Heavner, L. Hollberg, W. M. Itano, S. R. Jefferts, M. J. Delaney, K. Kim, F. Levi, T. E. Parker, and J. C. Bergquist. Single-atom optical clock with high accuracy. *Physical Review Letters*, 97(2), 2006.

[75] M. Kumagai, H. Ito, M. Kajita, and M. Hosokawa. Evaluation of caesium atomic fountain NICT-CsF1. *Metrologia*, 45(2):139–148, 2008.

[76] A Thompson and D Lampard. A new theorem in electrostatics and its application to calculable standards of capacitance. *Nature*, 177(4515):888–888, 1956.

[77] D. J. Thouless. Topological interpretations of quantum hall conductance. *Journal of Mathematical Physics*, 35(10):5362–5372, 1994.

[78] Beat Jeckelmann, Blaise Jeanneret, and Dave Inglis. High-precision measurements of the quantized hall resistance:experimental conditions for universality. *Physical Review B*, 55: 13124–13134, 1997.

[79] A. Hartland, K. Jones, J. M. Williams, B. L. Gallagher, and T. Galloway. Direct comparison of the quantized hall resistance in gallium arsenide and silicon. *Physical Review Letters*, 66:969–973, 1991.

[80] K. S. Novoselov, Z. Jiang, Y. Zhang, S. V. Morozov, H. L. Stormer, U. Zeitler, J. C. Maan, G. S. Boebinger, P. Kim, and A. K. Geim. Room-temperature quantum hall effect in graphene. *Science*, 315(5817):1379, 2007.